Cluster Catalysis with Lattice Oxygen: Tracing Oxygen Transport from a Magnetite (001) Support onto Small Pt Clusters

Sebastian Kaiser, Farahnaz Maleki, Ke Zhang, Wolfgang Harbich, Ueli Heiz, Sergio Tosoni, Barbara A. J. Lechner,* Gianfranco Pacchioni, and Friedrich Esch

Cite This: *ACS Catal.* 2021, 11, 9519–9529

Read Online

ACCESS | Metrics & More | Article Recommendations | Supporting Information

ABSTRACT: Oxidation catalysis on reducible oxide-supported small metal clusters often involves lattice oxygen. The present work aims at differentiating whether the reaction takes place at the cluster/support interface or on the cluster. To that purpose, we trace the path of lattice oxygen from $Fe_3O_4(001)$ onto small Pt clusters during the CO oxidation. While oxygen vacancies form on many other supports, magnetite maintains its surface stoichiometry upon reduction thanks to high cation mobility. To investigate whether size-dependent oxygen affinities play a role, we study two specific cluster sizes, Pt_5 and Pt_{19}. By separating different reaction steps in our experiment, migrating lattice oxygen can be accumulated on the clusters. Temperature-programmed desorption (TPD) and sophisticated pulsed valve experiments indicate that CO oxidation occurs with this highly reactive oxygen on the Pt clusters. Scanning tunneling microscopy (STM) shows a decrease in the apparent height of the clusters, which density functional theory (DFT) explains as a restructuring following lattice oxygen reverse spillover.

KEYWORDS: *size-selected clusters, lattice oxygen reverse spillover, Mars van Krevelen mechanism, magnetite, platinum, pulsed reactivity, STM, DFT*
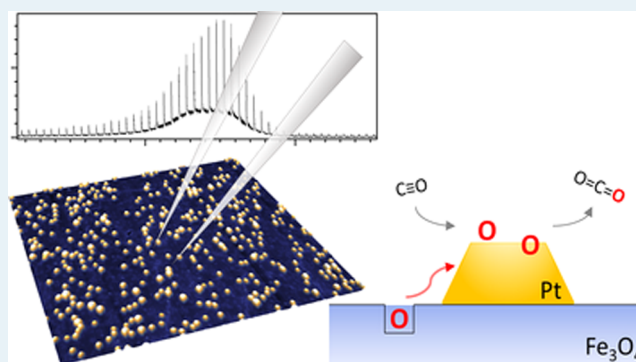
1. INTRODUCTION

From fine chemical synthesis over combustion control to electrode design, about 80% of industrial chemical processes rely on catalysts to improve energy and material efficiency,[1] of which about 90% are catalyzed heterogeneously.[2] Such a heterogeneous catalyst typically consists of small metal nanoparticles (several hundreds to thousands of atoms) or clusters (often defined as ≤100 atoms) dispersed on oxidic support materials.[3,4] In contrast to the bulk and large nanoparticles, small clusters exhibit discrete electronic states comparable to molecules, and therefore develop unique, strongly size-dependent chemical and physical properties. Small Pt clusters, for example, exhibit a nonmetallic behavior.[5] These properties can even change the catalytic behavior: Au, which is inert in the bulk state, becomes highly active and selective for redox catalysis.[6−8] In small particles, a large proportion of atoms is in direct contact with the underlying support, which can strongly influence their catalytic performance and stability. It can alter the catalytic activity of the particles indirectly,[9,10] itself being an integral part of the catalytic cycle,[11] and even encapsulate the particle in the strong metal−support interaction (SMSI),[12−14] thereby reducing[15] or enhancing[16] the catalytic activity.

In the case of CO oxidation on supported metal clusters, several reaction mechanisms have been distinguished based on the oxygen supply. When clusters are supported on non-reducible oxides, the CO oxidation typically takes place in a Langmuir−Hinshelwood mechanism, where CO and O_2 coadsorb from the gas phase and react.[17,18] On reducible oxide-supported clusters, on the other hand, the support can contribute lattice oxygen in a Mars van Krevelen (MvK) mechanism, thus not only providing a large oxygen reservoir but potentially also causing the entire catalyst system to restructure continuously.[19,20] The removal of lattice oxygen typically requires thermal activation, which can be facilitated in proximity to the clusters in a so-called metal-assisted MvK mechanism.[21] The resulting oxygen vacancies subsequently have to be refilled by gas-phase O_2 to complete the catalytic cycle. A central question remains whether the oxidation step takes place at the cluster/support interface or on the cluster.
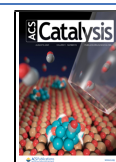
For larger nanoparticles, on supports such as ceria[22,23] and $Co_3O_4(111)$,[24] it was demonstrated that the reaction takes place on the particles via an oxygen reverse spillover, i.e., lattice oxygen transport onto the particles, which we will thus refer to as "lattice oxygen reverse spillover". In contrast to this oxygen originating from the lattice, classical reverse spillover typically involves species originating from the gas phase that first adsorb on the support and subsequently migrate to the catalytic sites.[25]

Here, we study a similar CO oxidation catalyst with two important differences. We use small monodisperse clusters at the extreme low end of the size scale (namely, Pt_5 and Pt_{19}) and deposit them on a magnetite, $Fe_3O_4(001)$, support, where we expect the oxygen exchange to be influenced by high cation mobility. While oxygen vacancies created on the above-mentioned supports need to be refilled from the gas phase, magnetite can maintain its surface stoichiometry by facile iron diffusion into the bulk,[26] thus providing a flexible oxygen reservoir. Magnetite is a magnetic, abundant, and reducible metal oxide, which crystallizes in an inverse spinel structure with Fe^{2+} occupying octahedral sites and Fe^{3+} occupying tetrahedral and octahedral sites in a 1:1 ratio, within an fcc-O^{2-} anion lattice.[27−29] Its (001) surface reconstructs into the subsurface cation vacancy (SCV) structure, whereby only Fe^{3+} occurs in the uppermost layers, yielding a $(\sqrt{2} \times \sqrt{2})R45°$ reconstruction.[30] In a scanning tunneling microscope (STM), this structure is observed in the form of parallel, undulating rows of iron atoms in octahedral sites, rotated 90° between adjacent terraces. The $Fe_3O_4(001)$ surface is rich in surface defects such as surface hydroxyls, antiphase domain boundaries (APDB) between the two reconstruction domains, or Fe-rich point defects such as unreconstructed unit cells and Fe adatoms.[31−34] These defects also act as adsorption and dissociation sites, thus participating in the surface chemistry.[35−37]

In the present work, we combine a multimodal experimental approach comprising scanning tunneling microscopy (STM), temperature-programmed desorption (TPD), and highly sensitive pulsed-reactivity experiments with state-of-the-art density functional theory (DFT) calculations to investigate a $Pt_n/Fe_3O_4(001)$ model catalyst during exposure to a CO oxidation reaction environment. We demonstrate lattice oxygen reverse spillover onto the small Pt clusters, observe a size dependence of CO poisoning, and identify an oxygen-induced restructuring of the clusters.

2. METHODS

2.1. Experimental Methods. Naturally grown $Fe_3O_4(001)$ samples (SurfaceNet GmbH) were prepared by several preparation cycles, each consisting of 20 min Ar^+ ion sputtering at room temperature (4×10^{-5} mbar Ar, 1 keV, 3.6 μA sputter current), followed by annealing in 5×10^{-7} mbar O_2 at 983 K. This procedure yields a reproducible and clean surface, which was checked for stoichiometry as well as carbon impurities using X-ray photoelectron spectroscopy (XPS) and STM on a regular basis. For heating, a boron nitride heater located directly in the sample holder in contact with the sample was used; the temperature was measured by a type K thermocouple directly attached to the crystal.

Size-selected Pt clusters were generated by a laser ablation source.[38] Pt is evaporated from a rotating target using the second harmonic of a pulsed Nd:YAG laser; the resulting plasma is subsequently cooled in the adiabatic expansion of a

He pulse (Westfalen AG, grade 6.0). This yields a supersonic beam of clusters, which is focused by several electrostatic lenses and guided toward a 90° quadrupole bender for positive charge selection. The resulting beam is mass-selected by a quadrupole mass filter and subsequently soft-landed on the substrate (i.e., with a kinetic energy <1 eV/atom). The clusters were deposited at room temperature. For TPD and reactivity measurements, a cluster density of 0.05 clusters/nm² was used, and for STM, a lower cluster coverage of 0.01 clusters/nm² allowed optimal evaluation of the terrace background around each cluster.

All experiments were carried out under ultrahigh vacuum (UHV) conditions, with a system base pressure of $<1 \times 10^{-10}$ mbar. All STM measurements were performed in constant current mode with a commercial Omicron VT-SPM instrument using electropolished Pt/Ir tips (Unisoku). STM image processing was performed with Gwyddion[39] using plane subtraction and row by row alignment tools for background correction. The height distribution of the particles was determined using a home-written Igor routine by the detection of the particles via an intensity threshold, drawing a profile through the cluster maximum and determining the height of the cluster with respect to its surrounding background.

The experimental setup was recently equipped with a device for high sensitivity TPD and reactivity measurements, the so-called sniffer, which was built adapting a design by Bonanni et al.[40] In short, this device combines a pulsed reactant doser with a differentially pumped quadrupole mass spectrometer (QMS, Pfeiffer Vacuum GmbH, QMA 200 Prisma Plus). Up to two different reactants can be pulsed independently. The reactants as well as the desorption and reaction products are guided using a heated quartz tube assembly. As the distance between the sniffer entrance and the sample is typically in the range of only ∼100−200 μm, the investigated surface is sufficiently decoupled from the rest of the chamber; thus, a high amount of reactant can be dosed while keeping UHV conditions in the surrounding chamber. In the present study, each pulse corresponded to a dosage of approximately 0.1 L. This decoupling in combination with the guiding tubes results in the vast majority of the desorption and reaction products reaching the QMS, yielding a very high sensitivity, as well as the spectra being free of any additional peaks caused by desorption from, e.g., the sample holder or the manipulator. The TPD and pulsed-reactivity experiments were carried out using O_2 (Westfalen AG, grade 5.0) and $C^{18}O$ (Eurisotop, 96.1%). All reactivity and TPD-related samples have been saturated with $C^{18}O$ during cluster deposition to gain control over the CO species adsorbed on the clusters despite CO being codeposited as a molecular beam during deposition with our cluster source. The delay between the pulses during the reactivity measurements was 4 s for O_2, 2.5 s for $C^{18}O$, and 2.5 s when pulsing O_2 and $C^{18}O$ alternatingly. The evaluation of the pulsed-reactivity data was carried out using a Matlab-based evaluation tool that differentiates between pulse-related gas signals and background by detecting single peaks and evaluating in a pre-set time window. The thus-determined background comprises offsets, desorption signals, initial pulse valve transients, and reactivity linked to long residence times and is subtracted; afterward, each pulse is integrated numerically. For details, see Figure S1 in the Supporting Information (SI).

2.2. Computational Models and Methods. DFT calculations have been performed to model the lattice oxygen reverse spillover process. To this end, we considered a Pt_5

cluster supported on the $Fe_3O_4(001)$ surface, Pt_5/Fe_3O_4, where a single cluster size is considered. In a real heterogeneous catalyst consisting of supported metal nanoparticles, the overall performance results from the convolution of the individual clusters activities; results obtained for a single cluster size may differ, at least quantitatively, from those of the real catalyst.[41] However, in this study, we are considering mass-selected, monodispersed Pt clusters, in particular Pt_5 and Pt_{19}, to be able to specifically compare experimental results with DFT models on exactly the same cluster size.

For the calculations, we used the code VASP 5.[42] The core electrons are described with the projector-augmented wave method.[43,44] O(2s, 2p), Fe(3s, 3p, 3d, 4s), and Pt(5d, 6s) electrons are treated explicitly. Spin-polarized calculations are carried out at the level of the generalized gradient approximation (GGA) adopting the Perdew, Burke, and Ernzerhof (PBE) exchange−correlation functional;[45] the exact values might vary slightly with the use of different functionals.[46] The strongly correlated character of Fe(3d) electrons is accounted for as in the GGA + U approach[47,48] by applying a Hubbard U parameter of 3.8 eV to the Fe 3d states.[30] The magnetic structure of Fe_3O_4 is correctly reproduced. Long-range dispersion is included according to the D3 method introduced by Grimme.[49] The relaxation of the magnetite bulk lattice parameters and internal coordinates has been performed with a $3 \times 3 \times 3$ K-point grid and a kinetic energy cutoff of 600 eV. All subsequent calculations on the (001) surface have then been carried out with a $2 \times 2 \times 1$ K-point grid and a kinetic energy cutoff of 400 eV. The calculations on the gas phase Pt clusters are carried out in Γ point only in a cubic 25 Å box. The truncation criteria for the electronic and ionic loops are 10^{-5} eV and 10^{-2} eV/Å, respectively. Kinetic barriers are calculated according to the climbing image-nudged elastic band approach,[50] considering four images along the reaction path.

The (001) surface of the magnetite is modeled by a $(\sqrt{2} \times \sqrt{2})R45°$ $Fe_{35}O_{48}$ slab, according to the subsurface-vacancy model formerly proposed by Parkinson and co-workers.[30] Further details on the model structures are reported in Section S2 of the SI.

To model the formation of an O vacancy, we distinguish three nonequivalent oxygen lattice positions on the $Fe_3O_4(001)$ surface. O1 and O2 lie on threefold-coordinated surface sites connecting Fe atoms in tetrahedral positions. O3 lies on top of an Fe ion in an octahedral site (see Figure S4). The thermodynamic stability of the O vacancy (estimated with respect to the pristine surface and $1/2$ O_2) depends on the site where the oxygen atom is removed. In particular, O3 located on top of Fe ions in octahedral sites can be removed at a cost of 2.91 eV; removal of O2 (3.10 eV) and O3 (3.55 eV) requires more energy (see also Section S3, SI).

3. RESULTS AND DISCUSSION

To identify how CO binds to $Pt_n/Fe_3O_4(001)$ and whether it reacts with lattice oxygen, we start with a discussion of the TPD spectra of CO-saturated surfaces without an external oxygen supply. Subsequently, the reactivity linked with either the CO or O_2 reactant is monitored by pulsed-reactivity measurements. A low-temperature reaction peak demonstrates that the lattice oxygen reverse spillover leads to a highly reactive oxygen species on the cluster. Finally, we will show that the lattice oxygen reverse spillover leads to structural changes of the clusters. We should note at this point that over

the entire temperature range discussed below, STM indicates that the cluster coverage remains constant and the distribution monodisperse. In the following, ripening can thus be excluded from the discussion. To define the terminology concerning the coordination of oxygen used in the following, we discriminate between oxygen adsorbed (a) on top of the cluster (i.e., only coordinated to Pt), (b) on the cluster (i.e., coordinated to Pt, but not necessarily exclusively so), (c) at the rim or the interface (i.e., coordinated to both Pt and Fe), and (d) in the periphery (i.e., somewhere around the cluster).

3.1. Setting the Stage: CO Oxidation in TPD Measurements. Figure 1a shows CO desorption curves from Pt_5 (orange) and Pt_{19} clusters (gray) deposited onto the $Fe_3O_4(001)$ surface. First, Pt_{19} clusters exhibit a broad desorption feature with an onset temperature of around 350
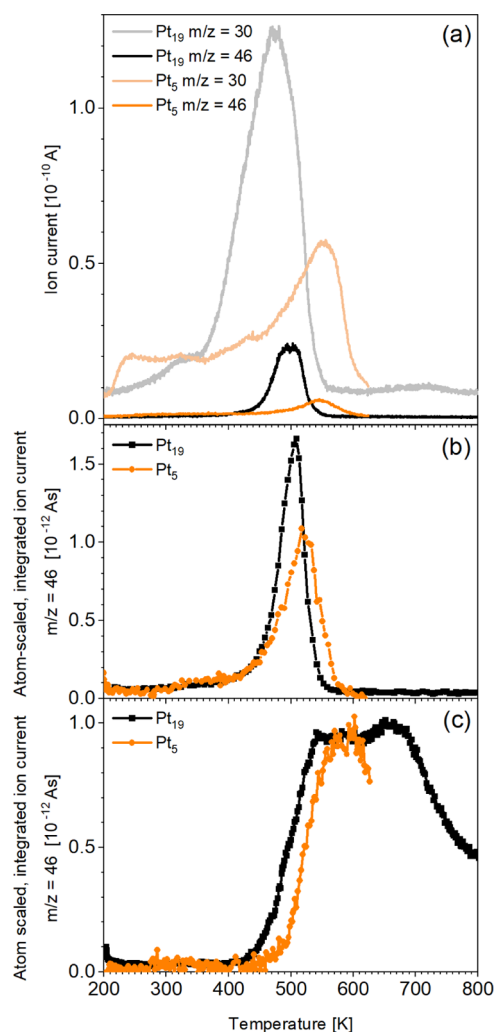

Figure 1. TPD and pulsed-reactivity spectra of Pt_{19} (black, gray) and Pt_5 (orange) supported on $Fe_3O_4(001)$. Using the same cluster density of 0.05 clusters/nm², the resulting atom density is ~4 times higher for the Pt_{19} sample. (a) Saturation TPD curves of $C^{18}O$ adsorbed at 200 K. The $C^{18}O$ ($m/z = 30$) and $C^{18}O^{16}O$ ($m/z = 46$) traces are shown. (b) $C^{18}O^{16}O$ ($m/z = 46$) production as a function of temperature, synchronized with O_2 reactant pulses on $C^{18}O$-saturated samples. (c) $C^{18}O^{16}O$ ($m/z = 46$) formation synchronized with $C^{18}O$ reactant pulses on $C^{18}O$-saturated samples. The heating rate was 1 K/s. All pulsed data were integrated and normalized to the number of Pt atoms per cluster.

K and a peak temperature of 475 K. This feature is not observed on the bare magnetite surface (see Figure S5 in the SI), agrees with the temperature range reported for CO desorption from Pt nanoparticles on $Fe_3O_4(001)$,[51] and can therefore be assigned to the clusters. Second, the weak and broad feature with a maximum at 710 K is similar to the CO recombinative desorption from Fe(111).[52] We thus conclude that it results from CO, which has been adsorbed dissociatively on the small number of highly reduced iron sites, most likely Fe adatoms, which are common defects on the $Fe_3O_4(001)$ surface.[31] Finally, there is another small feature around 330 K. Such features have been tentatively assigned in the literature to reduced iron sites that surround Pt nanoparticles on $Fe_3O_4(111)$ when the strong metal−support interaction sets in.[53] While this interaction requires higher temperatures not yet reached here, there could already be clusters present in close proximity to reduced iron defects.

The CO desorption features of Pt_5 are comparable to those of Pt_{19}, with the difference that the desorption maxima are shifted to higher temperatures, indicating stronger binding. Note that all Pt_5 measurements end at 625 K, as cluster ripening was observed in STM when heating to higher temperatures (see Figure S6). The main CO desorption feature from Pt_5 with an onset at around 420 K and a peak at 550 K is assigned to the clusters. A lower temperature feature at around 430 K is observed, comparable to the one observed at 330 K for Pt_{19}. For both cluster sizes, this feature is located around the onset temperature of the main desorption peak, i.e., both features are shifted similarly. This might indicate a similar origin of the lower temperature feature, namely, due to clusters in the vicinity of reduced surface defect sites.

In both samples, we observe weak desorption signals in the temperature range <300 K, which we assign to desorption from defects in the magnetite support (see TPD for bare magnetite in Figure S5).[35] Since their intensity decreases upon cluster deposition, we conclude that a significant part of the clusters is most likely located on surface defect sites such as unreconstructed unit cells or antiphase domain boundaries.[31,54] Note that the background at these low temperatures varies with the state of the single crystal, which we suspect is due to slight changes in sample cleanliness, oxidation state, and/or defect density. The measurements comparing bare and cluster-covered magnetite were therefore recorded in a close temporal sequence.

Having understood the CO features, we can now interpret the $C^{18}O^{16}O$ production signals recorded simultaneously with the CO desorption (also shown in Figure 1a). Since no oxygen is dosed, this CO_2 production, observed for both cluster sizes, must be strictly related to the availability of lattice oxygen for reaction with CO. During the TPD measurements, only $C^{18}O^{16}O$ and no $C^{18}O_2$ is observed, excluding a Boudouard-type reaction $(2CO \rightarrow C + CO_2)$. We are thus observing a MvK reaction. For Pt_{19}, the CO_2 feature has an onset temperature located at around 400 K and a broad peak at 500 K. Pt_5 exhibits a similar feature, starting below 420 K with the peak at 545 K. Note that we observe a change in the apparent cluster height in the same temperature range in STM measurements, as will be discussed later. As no CO_2 desorption could be detected for the bare $Fe_3O_4(001)$ surface (see Figure S5), we attribute the CO_2 signals to the presence of the clusters. For both cluster sizes, they exhibit about the same onset temperature and peak position with respect to the

corresponding CO desorption peaks, indicating that the CO_2 formation is closely related to the CO desorption.

3.2. Exploring the Reaction Mechanism by Overcoming Reactant Limitations: Pulsed-Reactivity Measurements. Complementary to the TPD experiments, we performed pulsed valve experiments that give access to the reaction rate synchronized with a given reactant pulse. In these background-corrected measurements (see Section S1), each data point is the integral over a product pulse and correlates with the reaction rate at a given temperature. These reactant-synchronized pulsed measurements allow us to investigate adsorption limitations, (i) of oxygen adsorption by CO poisoning (in pulsed O_2 experiments) and (ii) of CO adsorption at high temperatures (in pulsed CO experiments).

We start with pulsing O_2 onto the CO precovered sample and observe the CO_2 production shown in Figure 1b for Pt_5 (orange) and Pt_{19} clusters (black). The CO_2 formation starts around 400 K for both cluster sizes and peaks at 505 K for Pt_{19} and 520 K for Pt_5, respectively. This difference reflects the slightly higher binding energy of CO on Pt_5. While the cluster surface is poisoned with CO at low temperatures, binding sites for dissociative O_2 adsorption become available above the onset temperature of CO desorption, leading to the coadsorption of oxygen and CO on the same cluster.[18] At this temperature, the CO oxidation in a classical Langmuir−Hinshelwood manner is already facile on clusters,[55] and hence a high reaction rate is observed as soon as the adsorption limitations are overcome. The similarity to the CO_2 production in the TPD indicates that it is adsorption-limited as well. As we will discuss in detail in Section 3.5, DFT confirms that the activation barrier for the initial lattice oxygen reverse spillover is below 1 eV, hence far less than the CO binding energy calculated, e.g., for Pt_2 clusters on $Fe_3O_4(001)$.[56]

We note that the CO_2 production peak on Pt_5 in the pulsed experiments is at a somewhat lower temperature than the peak observed in TPD, contrary to Pt_{19}. This observation can be explained by a reaction limitation due to a lack of CO, which is not replenished during the measurement. When supplying CO by alternating CO and O_2 pulses (see Figure S7), the CO_2 formation synchronized with the O_2 pulses follows the shape of the corresponding CO_2 TPD trace, with the same onset and peak temperatures, thus confirming the hypothesis above.

We now describe the opposite experiment, pulsing CO without providing any oxygen. Figure 1c shows the CO_2 production observed for both investigated cluster sizes as a function of temperature. For Pt_{19}, CO_2 formation starts at around 425 K, reaching a plateau between 550 and 670 K with an approximately constant CO_2 formation rate. On Pt_5, an onset temperature of 450 K is observed, with a maximum at 590 K. This experiment allows probing the behavior of the CO_2 formation over a wider temperature range since the reactant is refreshed continuously by pulses and thus also available beyond the CO desorption temperature. As expected, the CO_2 production starts at the onset temperature of CO_2 formation in the TPD experiment, for both cluster sizes, although at a slightly higher temperature, where oxygen migration onto the cluster is no longer hindered by CO. The signal saturates once all available cluster sites can accommodate reactive oxygen atoms. This temperature coincides with the temperature where CO desorption is complete. Interestingly, the normalized peak intensity is the same for both cluster sizes. The number of active sites hence scales with the surface and not the rim of the cluster.[57] The upper limit of

the plateau could be due to encapsulation effects or due to limited oxygen coverage: chemisorption on stepped Pt(112) leads to O_2 desorption just below 700 K.[58] All of the plateau characteristics point to a reaction that is limited by free adsorption sites on the cluster surface and that also proceeds on the cluster, via lattice oxygen reverse spillover. In contrast, an interface reaction would not saturate as long as CO (and lattice oxygen) are available since the two reactants do not compete for adsorption sites.

3.3. Lattice Oxygen Reverse Spillover in Sequential CO TPDs.
Having shown the ease of lattice oxygen reverse spillover once adsorption sites are available, we now use this highly reactive oxygen species in a low-temperature reaction. We know from the literature that the CO oxidation on Pt clusters after sequential adsorption of oxygen and CO already takes place below 400 K.[18,55]

In the experiment in Figure 2, we show that it is indeed possible to observe an additional CO_2 production feature when
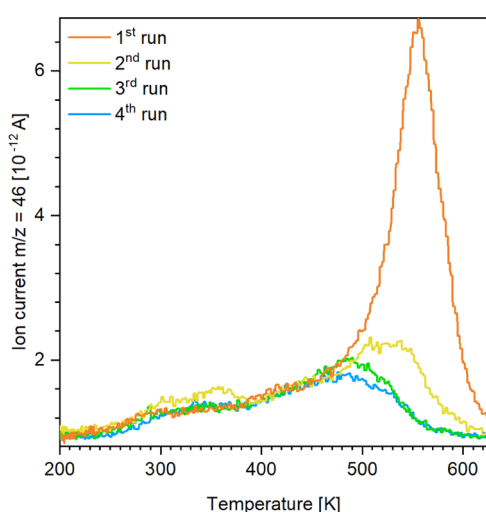
Figure 2. $C^{18}O^{16}O$ ($m/z = 46$) formation in subsequent CO-TPD spectra of Pt_5 supported on Fe_3O_4(001). In each run, the surface is saturated with $C^{18}O$ at 200 K; the heating rate was 1 K/s. Only in the second run (yellow), a CO_2 production feature around 300−370 K is observed. The main feature above 500 K decreases during the first two runs. Figure S8 shows the corresponding $C^{18}O$ desorption signals.

populating the clusters with oxygen by reverse spillover prior to CO adsorption. Figure 2 shows a sequence of CO_2 production TPD curves on a Pt_5 sample, each taken after saturating the surface with CO at 200 K. Remarkably, the anticipated low-temperature CO_2 feature around 300−370 K is observed only for one out of four runs, the second one. In the first run, CO poisoning and an activation barrier initially hinder oxygen migration onto the cluster and subsequently lead to high-temperature CO_2 formation. In contrast, the second run already starts with a certain coverage of reactive oxygen on the clusters, accumulated from lattice oxygen reverse spillover during the first temperature ramp after complete CO removal, which requires heating to beyond 550 K. At this high-temperature end of the TPD, however, cluster encapsulation due to SMSI starts as well, an effect that strongly affects the cluster reactivity, as studied for nanoparticles,[51] while requiring further investigation for clusters. Here, it leads to the well-known loss of CO adsorption capability that we see in the corresponding series of CO TPDs (see Figure S8). It is,

therefore, experimentally impossible to fully disentangle lattice oxygen reverse spillover from the onset of encapsulation. As a consequence, the low-temperature CO_2 production is not repeated in the third and fourth run. Only in the second run, we reach a starting situation where the cluster is CO-free, while the encapsulation is still incomplete. Note that the low intensity of the resulting low-temperature CO_2 production feature is likely caused by this partial encapsulation. Summing up, this experiment provides direct proof for reverse spillover of lattice oxygen.

3.4. Effects of the Lattice Oxygen Reverse Spillover on the Cluster Structure: STM Measurements.
In the following, we focus on the effects of this lattice oxygen reverse spillover on the cluster structure concerning the geometry and electronic state. Figure 3a−e shows a series of STM images displaying Pt_{19} clusters on a defect-rich Fe_3O_4(001) surface, recorded at the temperatures indicated in the figure. The clusters appear as bright protrusions on the surface and seem to be largely randomly distributed while maintaining their size upon deposition. At all temperatures investigated here, the clusters are still monodisperse; ripening or disintegration is not observed. At 473 K and even more pronounced at 573 K, tiny holes form around some of the clusters, but not all (details see Figure S9). Such holes are typically observed on this surface when oxygen atoms are removed, leaving behind under-coordinated iron atoms that diffuse into the bulk.[20] This is a direct consequence of the lattice oxygen reverse spillover occurring in the periphery of the clusters. The hole formation is more or less pronounced depending on the amount of CO in the chamber background that reacts off oxygen from the clusters, creating free adsorption sites for renewed oxygen migration.

Upon annealing, the cluster brightness seems to decrease, indicating a decline in their apparent height, while the coverage remains constant (confirmed by statistical analysis of several images of the same sample at different temperatures). This finding is quantified in Figure 3f for Pt_{19}, where the cluster height distributions at different temperatures are presented in histograms. Dashed red lines are used to indicate the approximate correspondence to atomic layers. While the Pt_{19} clusters are about three atomic layers high at room temperature, they flatten to between one and two layers at 573 K. The transition takes place between 423 and 523 K, which is the temperature range where CO_2 formation is observed in Figure 1a. This strong correlation in temperature suggests that the change in apparent height is caused by lattice oxygen reverse spillover.

When comparing several cluster sizes in Figure 3g, we find that this is a common phenomenon. The decrease in apparent height holds for all investigated cluster sizes, suggesting the lattice oxygen reverse spillover to be a universal effect for the Pt_n/Fe_3O_4(001) system. Such a behavior could either be explained by a real geometry change of the clusters or by a change in the density of states due to oxygen adsorption.

3.5. DFT Calculations Reveal Further Mechanistic Details.
The experimental results point to some mechanistic aspects that require theoretical investigation. In particular, we consider the following questions: (i) How easy is it to remove lattice oxygen from bare magnetite vs in the periphery of a cluster? (ii) Is lattice oxygen reverse spillover endo- or exothermic, and can we confirm that the clusters can be covered by considerable amounts of oxygen? (iii) What is the
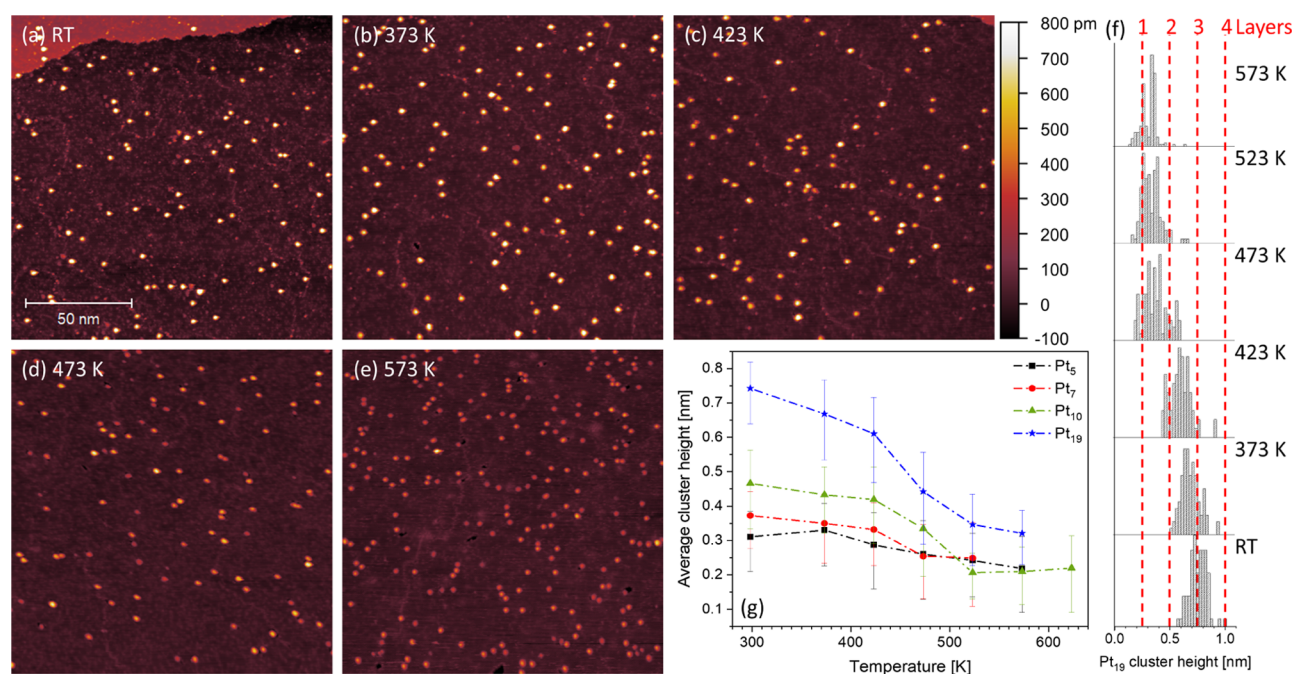
Figure 3. Height evolution of $Pt_n/Fe_3O_4(001)$ as a function of temperature. (a–e) STM images (150×150 nm^2) of Pt_{19} clusters (0.01 clusters/nm^2) measured at the temperatures indicated. All images have been scaled to the same false color scale for height comparison. Note that (e) is from a second set of experiments with a slightly higher cluster coverage than (a)–(d). The coverage in (e) is consistent with the coverage of the same sample after RT deposition. (f) Height profiles comparing the size distribution of Pt_{19} in (a)–(e) as a function of temperature. (g) Evolution of the average cluster height as a function of temperature for Pt_5, Pt_7, Pt_{10}, and Pt_{19}. Imaging parameters: $V_b = 1.50$ V; (a, e) $I_t = 300$ pA, (b–d) $I_t = 400$ pA.
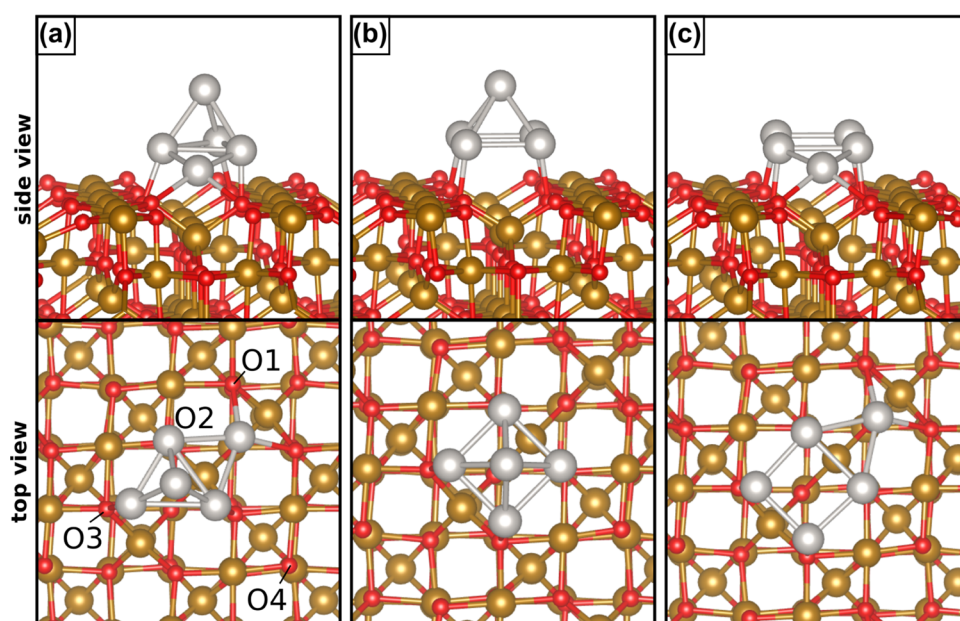
Figure 4. Pt_5 clusters on the $Fe_3O_4(001)$ surface. (a)–(c) are the three most stable isomers, with isomer (a) being 1.5 and 1.78 eV lower in energy than the isomers in (b) and (c), respectively. Red, brown, and gray spheres correspond to O, Fe, and Pt atoms, respectively.

activation barrier? (iv) Can the apparent height change in STM be explained by a restructuring?

First, we studied the structure of a gas phase Pt_5 cluster, starting from the most stable isomers reported in the literature.[59−65] This led to six isomers with very similar stability; the energy difference between the ground state and the least stable of the six isomers considered here is 0.35 eV, and sometimes different structures are separated by a few millielectronvolts, suggesting a fluxional behavior of the gas phase clusters (see Section S9, SI). Upon deposition on Fe_3O_4, some of the structures retain the topology of the gas phase, while others undergo a strong rearrangement. The Pt_5 adsorption energies (Table S4), computed with respect to $Fe_3O_4(001)$ and the most stable Pt_5 isomer (Pt_5 in Figure S10i), show that the ground state corresponds to a capped rhombus, with an adsorption energy of −4.51 eV, shown in
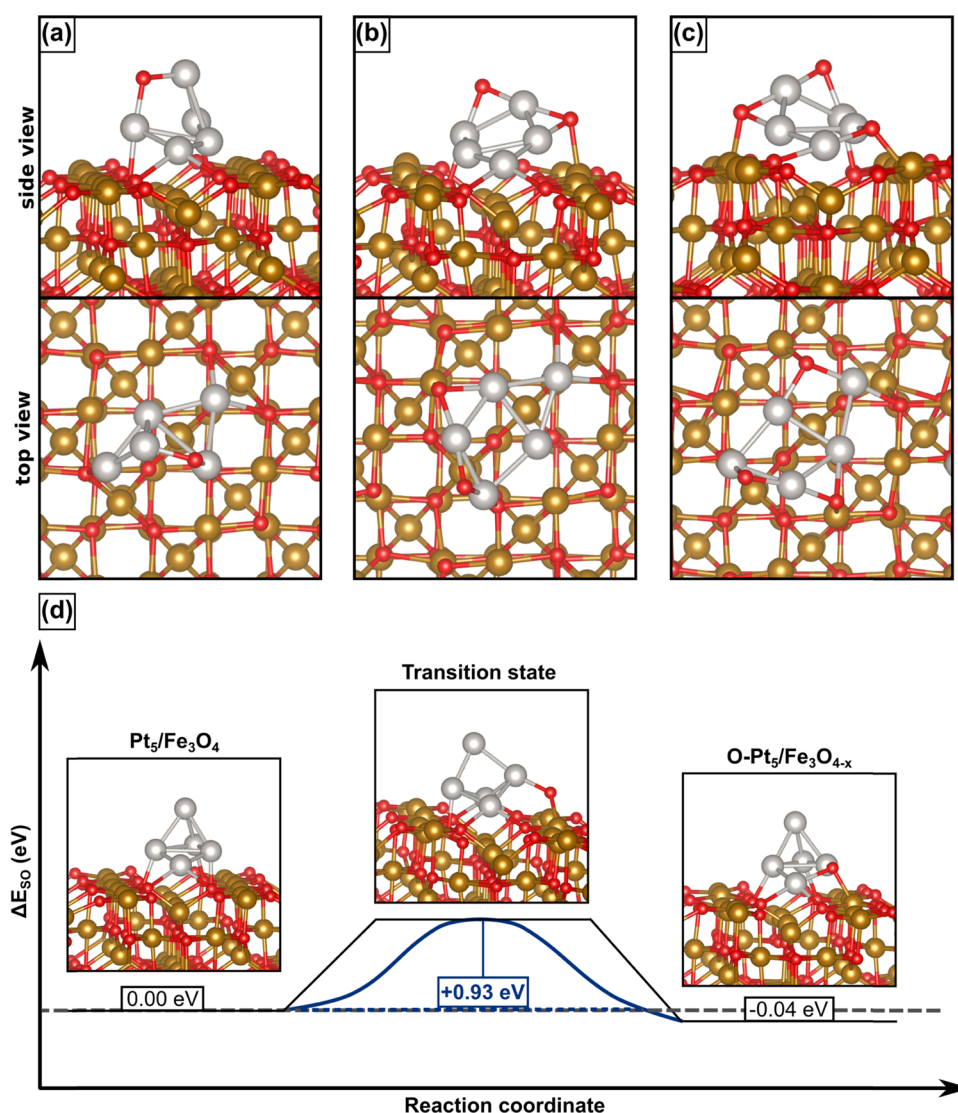
Figure 5. Side and top views of the most stable structures obtained for reverse spillover of (a) one, (b) two, and (c) three lattice oxygen atoms. In (d), the energy profile to displace an O atom from a lattice position to Pt$_5$ is shown.

Figure 4a, followed by a square pyramidal Pt$_5$ cluster (Figure 4b) and a planar structure (Figure 4c). Note that the most stable isomer, Figure 4a, is 1.5 eV more favorable than the next one, which shows that the surface has a strong stabilizing effect on this structure. This also suggests that the conversion of one isomer into another is much more difficult than in the gas phase.

Upon deposition, the Pt cluster becomes slightly positively charged (by 0.3 e) and a partial quenching of the magnetic moment of the support occurs, with a reduction from 3.3 μ_B per Fe$_3$O$_4$ formula unit in the clean surface to 2.59 μ_B when Pt$_5$ is adsorbed, as shown in Table S4.

We now start addressing question (i). The formation energy of an O vacancy on the clean Fe$_3$O$_4$(001) surface is about 3 eV (see Table S2 and Section S3). The addition of a metal/oxide interface may facilitate the removal of the O atoms in contact with the metal adduct.[21] We have explored this possibility by removing O atoms from four possible sites in the cluster periphery, indicated in Figure 4a, involving O either in direct contact with Pt$_5$ or at some distance. The formation energy of an O vacancy on Pt$_5$/Fe$_3$O$_4$ is reduced with respect to the clean surface. In particular, the formation of V$_{O2}$ has a cost of

1.98 eV, about 0.9 eV smaller than the most favorable case on the clean surface, which costs 2.91 eV. Also, the removal of an O atom not in direct contact with Pt$_5$ (such as V$_{O4}$) is slightly easier by almost 0.5 eV (see also Section S10, SI). These results point to a metal-assisted MvK mechanism.

In a second step, we address question (ii) regarding the endo-/exothermicity of the reverse spillover. The mechanism of lattice oxygen reverse spillover involves the displacement of O atoms from the lattice positions and their adsorption on the supported metal cluster. To model this process, we have started from the most favorable case of O removal (V$_{O2}$ in Figure 4a) and have readsorbed an O atom on various sites of Pt$_5$. A preliminary exploration of O adsorption on gas-phase Pt$_5$ provides information about the most stable adsorption sites (see Table S3). O adsorbs preferentially in a bridge mode or as a terminal Pt–O group, followed by threefold hollow sites. When the cluster is adsorbed on Fe$_3$O$_4$, additional adsorption sites are present at the Pt$_5$/Fe$_3$O$_4$ interface. In some cases, the lattice oxygen reverse spillover process is endothermic, but there are also structures where the product is more stable than the initial configuration. The most favorable case is shown in Figure 5a, where an O from the interface is inserted into a Pt–

Pt bond, which is preferred by −0.40 eV (see Table S6 and Figure S11 for further details). Thus, lattice oxygen reverse spillover involving a single O atom is thermodynamically favorable.

This leads us to question (iii) where we want to connect the lattice oxygen vacancy formation with the oxygen adsorption on the cluster by a viable path. This process is activated, and the kinetic barrier has been estimated for the initial step of the reaction, i.e., the displacement of an O atom from an O2 lattice site (see Figure 4a) to a nearby interfacial site where it binds at the cluster rim, shown in Figure 5. For this specific path, the whole process is almost thermoneutral, and the barrier of 0.93 eV can be overcome by thermal effects at the temperatures involved in the experiments described above. It is reasonable to assume that the displacement of the O atom from the lattice is the rate-determining step of the whole process: further diffusion of O-species on Pt_5 should occur with low barriers due to similar bond strengths of various adsorption sites.

Next, we have considered the case of the removal of a second O atom from various lattice sites and its readsorption on Pt_5O. Also, in this case, we found a few structures where the process is exothermic. The formation of the most stable isomer, shown in Figure 5b, where two O atoms are adsorbed on a bridge site, is exothermic by −0.64 eV (see also Table S7 and Figure S12). Finally, the process has also been considered for a third O atom, which is removed from the cluster/oxide interface and readsorbed on Pt_5, forming an oxidized Pt_5O_3-supported cluster, as shown in Figure 5c. This generates a large number of possible initial combinations, and we could explore only a few of them. In the most favorable case (Figure 5c), the transfer of three O atoms is slightly endothermic, by 0.17 eV only. We cannot exclude the existence of even more favorable isomers, and entropic effects are expected to further favor the process. This supports the evidence that multiple lattice oxygen reverse spillover from magnetite onto a Pt cluster is energetically accessible (for further details, see Figure S13 and Table S8).

This opens the question of the best channel for CO oxidation via CO reaction with an O atom of Fe_3O_4 at the interface of Pt_5 with the support or with the O atoms adsorbed on the Pt cluster. The experiments show a complex behavior as a function of CO poisoning, reaction temperature, cluster size, etc. and suggest that the number of active sites scales with the number of surface and not the rim atoms of the clusters. With our simplified models, we cannot determine active sites directly but instead compare the energy required to remove the three kinds of oxygen atoms present in the catalyst: lattice oxygen, Pt_5 rim oxygen, or oxygen present on top of the cluster. Oxygen removal from the lattice costs about 3 eV (Table S2 and Section S3). The removal of a lattice O atom from the periphery of the Pt_5/Fe_3O_4 cluster costs 2.0, 2.5, 2.7, and 3.1 eV (Table S5), depending on the site (on average 2.6 eV). These numbers can be compared to the cost of desorbing an O atom from Pt_5O supported on Fe_3O_{4-x}, where an O vacancy has been created. In the most stable configuration, the cost is 2.38 eV (see Figure S14), indicating that the Pt−O bond is strong and that at low O coverage, removing the O adatoms from a Pt cluster has a comparable cost to removing O atoms from the cluster/oxide interface. Next, we considered O removal from Pt_5O_2 (here, two O vacancies have been created on Fe_3O_4); removing the O atom bound only to the Pt_5 cluster costs 2.36 eV, while the removal of the O atom at the boundary with the oxide costs 2.22 eV (Figure S14). Things

change for even higher O coverages though. We have removed each of the three O atoms bound to Pt_5 in Pt_5O_3/Fe_3O_{4-3x}, and the cost is 1.72, 2.20, and 2.24 eV, respectively, Figure S14 (on average 2.05 eV). This suggests that for more pronounced lattice oxygen reverse spillover or higher O coverages on Pt clusters, the reaction of CO with adsorbed oxygen becomes preferred.

Finally, in question (iv), we want to rationalize the structural changes observed in the STM images. Lattice oxygen reverse spillover indeed induces a structural change in the supported cluster, as apparent in Figures 4 and 5. In particular, there is a tendency to rearrange the structure of Pt_5 from three-dimensional (3D) to a quasi-two-dimensional (quasi-2D) as the O loading increases. To quantify this effect, we have computed the average cluster height with respect to the Fe_3O_4 surface for all of the cases discussed here, and indeed there is an overall reduction of the cluster height (see Section S12, SI). This could indicate that the height evolution observed in STM, as shown in Figure 3, is due to geometry changes and not purely an electronic effect. At this point, we cannot fully rule out a thermal restructuring, leading to a change of the cluster structure.

Furthermore, Fe spillover from Fe_3O_4 onto Pt_5 and Pt_5O_3 has been considered, following a similar strategy as described above for lattice oxygen reverse spillover. In all cases considered, however, Fe reverse spillover is highly unfavorable (see Section S13, SI). Thus, if Fe diffusion occurs, this will be toward the bulk of magnetite, not toward the supported Pt clusters. These results suggest that the encapsulation of Pt clusters due to SMSI effects follows more complex paths than the diffusion of isolated Fe atoms.

4. CONCLUSIONS

A central question concerning cluster catalysis with lattice oxygen, in a Mars van Krevelen mechanism, is whether the reaction occurs at the cluster−support interface or whether the oxygen first migrates onto the cluster to react there. We studied this distinction on the example of metal-assisted MvK in the CO oxidation on small, size-selected Pt_n clusters supported on magnetite $Fe_3O_4(001)$ in a multimodal experiment, supported by DFT calculations. The detailed TPD and pulsed-reactivity experiments revealed a reaction on the cluster that involves reverse spillover of lattice oxygen, a phenomenon hitherto not reported on this support. Via annealing-induced migration, highly reactive lattice oxygen can be accumulated on the clusters and react in a low-temperature window of 300−370 K.

As our calculations for Pt_5 clusters showed, this reverse spillover process is exothermic for the first two oxygen atoms, with an initial migration activation barrier below 1 eV, much lower than the CO desorption barrier. Thus, the lattice oxygen reverse spillover is driven by overcoming CO poisoning and scales with the availability of free adsorption sites. The maximum obtainable turnover rates observed in the pulsed-reactivity experiments scale with the number of cluster surface atoms.

STM investigations showed that the clusters remain monodisperse throughout all experiments but with a distinct decrease in apparent height, concomitant to the formation of holes due to lattice oxygen removal. The calculations suggest that this change could be due to a true geometrical adaptation upon lattice oxygen reverse spillover, resulting in a transition from 3D to 2D clusters.

Larger Pt nanoparticles on the same support have been shown to become encapsulated by a thin, reduced iron oxide film due to SMSI.[51] In first experiments, we found this effect to also occur on small clusters, at temperatures where lattice oxygen reverse spillover already occurred. Calculations suggest that the growth of thin oxide films occurs through more complex paths than the mere diffusion of isolated Fe atoms, warranting more extensive future investigations.

■ ASSOCIATED CONTENT

Ⓢ Supporting Information

The Supporting Information is available free of charge at https://pubs.acs.org/doi/10.1021/acscatal.1c01451.

> Pulsed-reactivity data evaluation (Section S1); characterization of the magnetite bulk and (001) surface by DFT calculations (Section S2); formation of a surface oxygen vacancy on various sites (Section S3); CO desorption from bare magnetite and magnetite-supported clusters in TPD (Section S4); ripening of Pt_5 in STM (Section S5); alternating CO and O_2 pulses on $Pt_5/Fe_3O_4(001)$ (Section S6); loss of CO adsorption capability upon cluster encapsulation (Section S7); hole formation in cluster periphery (Section S8); platinum clusters in the gas phase: structure relaxation and oxygen adsorption (Section S9); adsorption of Pt_5 on $Fe_3O_4(001)$ and formation of oxygen vacancies (Section S10); lattice oxygen reverse spillover (Section S11); impact of lattice oxygen reverse spillover on cluster height (Section S12); and iron spillover (Section S13) (PDF)

■ AUTHOR INFORMATION

Corresponding Author

Barbara A. J. Lechner − *Chair of Physical Chemistry, Department of Chemistry, Technical University of Munich, 85748 Garching, Germany;* ⓘ orcid.org/0000-0001-9974-1738; Email: bajlechner@tum.de

Authors

Sebastian Kaiser − *Chair of Physical Chemistry, Department of Chemistry, Technical University of Munich, 85748 Garching, Germany; Catalysis Research Center, Technical University of Munich, 85748 Garching, Germany*

Farahnaz Maleki − *Dipartimento di Scienza dei Materiali, University of Milano-Bicocca, 20125 Milano, Italy;* ⓘ orcid.org/0000-0002-5747-1319

Ke Zhang − *Chair of Physical Chemistry, Department of Chemistry, Technical University of Munich, 85748 Garching, Germany; Catalysis Research Center, Technical University of Munich, 85748 Garching, Germany*

Wolfgang Harbich − *Institute of Physics, Ecole Polytechnique Fédérale de Lausanne, CH-1015 Lausanne, Switzerland;* ⓘ orcid.org/0000-0002-1515-151X

Ueli Heiz − *Chair of Physical Chemistry, Department of Chemistry, Technical University of Munich, 85748 Garching, Germany; Catalysis Research Center, Technical University of Munich, 85748 Garching, Germany;* ⓘ orcid.org/0000-0002-9403-1486

Sergio Tosoni − *Dipartimento di Scienza dei Materiali, University of Milano-Bicocca, 20125 Milano, Italy;* ⓘ orcid.org/0000-0001-5700-4086

Gianfranco Pacchioni − *Dipartimento di Scienza dei Materiali, University of Milano-Bicocca, 20125 Milano, Italy;* ⓘ orcid.org/0000-0002-4749-0751

Friedrich Esch − *Chair of Physical Chemistry, Department of Chemistry, Technical University of Munich, 85748 Garching, Germany; Catalysis Research Center, Technical University of Munich, 85748 Garching, Germany;* ⓘ orcid.org/0000-0001-7793-3341

Complete contact information is available at:
https://pubs.acs.org/10.1021/acscatal.1c01451

Notes

The authors declare no competing financial interest.
The structures of the calculations reported in this paper are available upon reasonable request to the authors.

■ ACKNOWLEDGMENTS

■ REFERENCES

(1) Ma, Z.; Zaera, F. Heterogeneous Catalysis by Metals. In *Encyclopedia of Inorganic Chemistry*, 2nd ed.; King, R. B., Ed.; John Wiley & Sons: Chichester, 2005; pp 1768−1784.

(2) Rothenberg, G. *Catalysis: Concepts and Green Applications*; Wiley-VCH: Weinheim, 2008; pp 129−131.

(3) Bell, A. T. The Impact of Nanoscience in Heterogeneous Catalysis. *Science* **2003**, *299*, 1688−1691.

(4) Schauermann, S.; Nilius, N.; Shaikhutdinov, S.; Freund, H. J. Nanoparticles for Heterogeneous Catalysis: New Mechanistic Insights. *Acc. Chem. Res.* **2013**, *46*, 1673−1681.

(5) Eberhardt, W.; Fayet, P.; Cox, D. M.; Fu, Z.; Kaldor, A.; Sherwood, R.; Sondericker, D. Photoemission from Mass-Selected Monodispersed Pt Clusters. *Phys. Rev. Lett.* **1990**, *64*, 780−783.

(6) Valden, M.; Lai, X.; Goodman, D. W. Onset of Catalytic Activity of Gold Clusters on Titania with the Appearance of Nonmetallic Properties. *Science* **1998**, *281*, 1647−1650.

(7) Sanchez, A.; Abbet, S.; Heiz, U.; Schneider, W.-D.; Häkkinen, H.; Barnett, R. N.; Landman, U. When Gold Is Not Noble: Nanoscale Gold Catalysts. *J. Phys. Chem. A* **1999**, *103*, 9573−9578.

(8) Bus, E.; Prins, R.; van Bokhoven, J. A. Origin of the Cluster-Size Effect in the Hydrogenation of Cinnamaldehyde over Supported Au Catalysts. *Catal. Commun.* **2007**, *8*, 1397−1402.

(9) Crampton, A. S.; Rotzer, M. D.; Landman, U.; Heiz, U. Can Support Acidity Predict Sub-Nanometer Catalyst Activity Trends? *ACS Catal.* **2017**, *7*, 6738−6744.

(10) Lee, S.; Lee, B.; Seifert, S.; Winans, R. E.; Vajda, S. Fischer-Tropsch Synthesis at a Low Pressure on Subnanometer Cobalt Oxide Clusters: The Effect of Cluster Size and Support on Activity and Selectivity. *J. Phys. Chem. C* **2015**, *119*, 11210−11216.

(11) Walenta, C. A.; Kollmannsberger, S. L.; Courtois, C.; Pereira, R. N.; Stutzmann, M.; Tschurl, M.; Heiz, U. Why Co-Catalyst-Loaded

Rutile Facilitates Photocatalytic Hydrogen Evolution. *Phys. Chem. Chem. Phys.* **2019**, *21*, 1491−1496.

(12) Tauster, S. J. Strong Metal-Support Interactions. *Acc. Chem. Res.* **1987**, *20*, 389−394.

(13) Dulub, O.; Hebenstreit, W.; Diebold, U. Imaging Cluster Surfaces with Atomic Resolution: The Strong Metal-Support Interaction State of Pt Supported on TiO2(110). *Phys. Rev. Lett.* **2000**, *84*, 3646−3649.

(14) Qin, Z. H.; Lewandowski, M.; Sun, Y. N.; Shaikhutdinov, S.; Freund, H. J. Encapsulation of Pt Nanoparticles as a Result of Strong Metal-Support Interaction with Fe3O4(111). *J. Phys. Chem. C* **2008**, *112*, 10209−10213.

(15) Polo-Garzon, F.; Blum, T. F.; Bao, Z.; Wang, K.; Fung, V.; Huang, Z.; Bickel, E. E.; Jiang, D.; Chi, M.; Wu, Z. In Situ Strong Metal−Support Interaction (SMSI) Affects Catalytic Alcohol Conversion. *ACS Catal.* **2021**, *11*, 1938−1945.

(16) Lewandowski, M.; Sun, Y. N.; Qin, Z. H.; Shaikhutdinov, S.; Freund, H. J. Promotional Effect of Metal Encapsulation on Reactivity of Iron Oxide Supported Pt Catalysts. *Appl. Catal., A* **2011**, *391*, 407−410.

(17) Kunz, S.; Schweinberger, F. F.; Habibpour, V.; Röttgen, M.; Harding, C.; Arenz, M.; Heiz, U. Temperature Dependent CO Oxidation Mechanisms on Size-Selected Clusters. *J. Phys. Chem. C* **2010**, *114*, 1651−1654.

(18) Heiz, U.; Sanchez, A.; Abbet, S.; Schneider, W. D. Catalytic Oxidation of Carbon Monoxide on Monodispersed Platinum Clusters: Each Atom Counts. *J. Am. Chem. Soc.* **1999**, *121*, 3214−3217.

(19) Widmann, D.; Behm, R. J. Activation of Molecular Oxygen and the Nature of the Active Oxygen Species for Co Oxidation on Oxide Supported Au Catalysts. *Acc. Chem. Res.* **2014**, *47*, 740−749.

(20) Bliem, R.; van der Hoeven, J.; Zavodny, A.; Gamba, O.; Pavelec, J.; de Jongh, P. E.; Schmid, M.; Diebold, U.; Parkinson, G. S. An Atomic-Scale View of CO and H2 Oxidation on a Pt/Fe3O4 Model Catalyst Angewandte. *Angew. Chem., Int. Ed.* **2015**, *127*, 13999−14002.

(21) Ruiz Puigdollers, A.; Schlexer, P.; Tosoni, S.; Pacchioni, G. Increasing Oxide Reducibility: The Role of Metal/Oxide Interfaces in the Formation of Oxygen Vacancies. *ACS Catal.* **2017**, *7*, 6493−6513.

(22) Zafiris, G. S.; Gorte, R. J. Evidence for Low-Temperature Oxygen Migration from Ceria to Rh. *J. Catal.* **1993**, *139*, 561−567.

(23) Happel, M.; Mysliveček, J.; Johánek, V.; Dvořák, F.; Stetsovych, O.; Lykhach, Y.; Matolín, V.; Libuda, J. Adsorption Sites, Metal-Support Interactions, and Oxygen Spillover Identified by Vibrational Spectroscopy of Adsorbed CO: A Model Study on Pt/Ceria Catalysts. *J. Catal.* **2012**, *289*, 118−126.

(24) Lykhach, Y.; Faisal, F.; Skála, T.; Neitzel, A.; Tsud, N.; Vorokhta, M.; Dvořák, F.; Beranová, K.; Kosto, Y.; Prince, K. C.; Matolín, V.; Libuda, J. Interplay between the Metal-Support Interaction and Stability in Pt/Co3O4(111) Model Catalysts. *J. Mater. Chem. A* **2018**, *6*, 23078−23086.

(25) Röttgen, M. A.; Abbet, S.; Judai, K.; Antonietti, J. M.; Wörz, A. S.; Arenz, M.; Henry, C. R.; Heiz, U. Cluster Chemistry: Size-Dependent Reactivity Induced by Reverse Spill-Over. *J. Am. Chem. Soc.* **2007**, *129*, 9635−9639.

(26) Arndt, B.; Lechner, B. A. J.; Bourgund, A.; Grånäs, E.; Creutzburg, M.; Krausert, K.; Hulva, J.; Parkinson, G. S.; Schmid, M.; Vonk, V.; Esch, F.; Stierle, A. Order-Disorder Phase Transition of the Subsurface Cation Vacancy Reconstruction on Fe3O4(001). *Phys. Chem. Chem. Phys.* **2020**, *22*, 8336−8343.

(27) Fleet, M. E. The Structure of Magnetite. *Acta Crystallogr., Sect. B: Struct. Crystallogr. Cryst. Chem.* **1981**, *37*, 917−920.

(28) Verwey, E. J. W.; Heilmann, E. L. Physical Properties and Cation Arrangement of Oxides with Spinel Structures I. Cation Arrangement in Spinels. *J. Chem. Phys.* **1947**, *15*, 174−180.

(29) Verwey, E. J.; Haayman, P. W.; Romeijn, F. C. Physical Properties and Cation Arrangement of Oxides with Spinel Structures II. Electronic Conductivity. *J. Chem. Phys.* **1947**, *15*, 181−187.

(30) Bliem, R.; McDermott, E.; Ferstl, P.; Setvin, M.; Gamba, O.; Pavelec, J.; Schneider, M. A.; Schmid, M.; Diebold, U.; Blaha, P.; Hammer, L.; Parkinson, G. S. Subsurface Cation Vacancy Stabilization of the Magnetite (001) Surface. *Science* **2014**, *346*, 1215−1218.

(31) Parkinson, G. S. Iron Oxide Surfaces. *Surf. Sci. Rep.* **2016**, *71*, 272−365.

(32) Parkinson, G. S.; Novotny, Z.; Argentero, G.; Schmid, M.; Pavelec, J.; Kosak, R.; Blaha, P.; Diebold, U. Carbon Monoxide-Induced Adatom Sintering in a Pd-Fe3O4 Model Catalyst. *Nat. Mater.* **2013**, *12*, 724−728.

(33) Novotny, Z.; Mulakaluri, N.; Edes, Z.; Schmid, M.; Pentcheva, R.; Diebold, U.; Parkinson, G. S. Probing the Surface Phase Diagram of Fe3O4(001) towards the Fe-Rich Limit: Evidence for Progressive Reduction of the Surface. *Phys. Rev. B* **2013**, *87*, No. 195410.

(34) Parkinson, G. S.; Novotný, Z.; Jacobson, P.; Schmid, M.; Diebold, U. A Metastable Fe(A) Termination at the Fe3O4(001) Surface. *Surf. Sci.* **2011**, *605*, L42−L45.

(35) Hulva, J.; Jakub, Z.; Novotny, Z.; Johansson, N.; Knudsen, J.; Schnadt, J.; Schmid, M.; Diebold, U.; Parkinson, G. S. Adsorption of CO on the Fe3O4(001) Surface. *J. Phys. Chem. B* **2018**, *122*, 721−729.

(36) Meier, M.; Hulva, J.; Jakub, Z.; Pavelec, J.; Setvin, M.; Bliem, R.; Schmid, M.; Diebold, U.; Franchini, C.; Parkinson, G. S. Water Agglomerates on Fe3O4(001). *Proc. Natl. Acad. Sci. U.S.A.* **2018**, *115*, E5642−E5650.

(37) Pavelec, J.; Hulva, J.; Halwidl, D.; Bliem, R.; Gamba, O.; Jakub, Z.; Brunbauer, F.; Schmid, M.; Diebold, U.; Parkinson, G. S. A Multi-Technique Study of CO2 Adsorption on Fe3O4 Magnetite. *J. Chem. Phys.* **2017**, *146*, No. 014701.

(38) Heiz, U.; Vanolli, F.; Trento, L.; Schneider, W. D. Chemical Reactivity of Size-Selected Supported Clusters: An Experimental Setup. *Rev. Sci. Instrum.* **1997**, *68*, 1986−1994.

(39) Nečas, D.; Klapetek, P. Gwyddion: An Open-Source Software for SPM Data Analysis. *Cent. Eur. J. Phys.* **2012**, *10*, 181−188.

(40) Bonanni, S.; Aït-Mansour, K.; Hugentobler, M.; Brune, H.; Harbich, W. An Experimental Setup Combining a Highly Sensitive Detector for Reaction Products with a Mass-Selected Cluster Source and a Low-Temperature STM for Advanced Nanocatalysis. *Eur. Phys. J. D* **2011**, *63*, 241−249.

(41) Zhang, Z.; Zandkarimi, B.; Alexandrova, A. N. Ensembles of Metastable States Govern Heterogeneous Catalysis on Dynamic Interfaces. *Acc. Chem. Res.* **2020**, *53*, 447−458.

(42) Kresse, G.; Furthmüller, J. Efficiency of Ab-Initio Total Energy Calculations for Metals and Semiconductors Using a Plane-Wave Basis Set. *Comput. Mater. Sci.* **1996**, *6*, 15−50.

(43) Blöchl, P. E. Projector Augmented-Wave Method. *Phys. Rev. B* **1994**, *50*, 17953−17979.

(44) Kresse, G.; Joubert, D. From Ultrasoft Pseudopotentials to the Projector Augmented-Wave Method. *Phys. Rev. B: Condens. Matter Mater. Phys.* **1999**, *59*, 1758−1775.

(45) Perdew, J. P.; Burke, K.; Ernzerhof, M. Generalized Gradient Approximation Made Simple. *Phys. Rev. Lett.* **1996**, *77*, 3865−3868.

(46) Pacchioni, G. Modeling Doped and Defective Oxides in Catalysis with Density Functional Theory Methods: Room for Improvements. *J. Chem. Phys.* **2008**, *128*, No. 182505.

(47) Anisimov, V. I.; Zaanen, J.; Andersen, O. K. Band Theory and Mott Insulators: Hubbard U Instead of Stoner I. *Phys. Rev. B* **1991**, *44*, 943−954.

(48) Dudarev, S.; Botton, G.; Savrasov, S. Y.; Humphreys, C. J.; Sutton, A. P. Electron-Energy-Loss Spectra and the Structural Stability of Nickel Oxide: An LSDA+U Study. *Phys. Rev. B: Condens. Matter Mater. Phys.* **1998**, *57*, 1505−1509.

(49) Grimme, S.; Antony, J.; Ehrlich, S.; Krieg, H. A Consistent and Accurate Ab Initio Parametrization of Density Functional Dispersion Correction (DFT-D) for the 94 Elements H-Pu. *J. Chem. Phys.* **2010**, *132*, No. 154104.

(50) Henkelman, G.; Uberuaga, B. P.; Jónsson, H. Climbing Image Nudged Elastic Band Method for Finding Saddle Points and Minimum Energy Paths. *J. Chem. Phys.* **2000**, *113*, 9901−9904.

(51) Zhang, K.; Shaikhutdinov, S.; Freund, H.-J. Does the Surface Structure of Oxide Affect the Strong Metal-Support Interaction with Platinum? Platinum on Fe3O4(001) versus Fe3O4(111). *ChemCatChem* **2015**, *7*, 3725−3730.

(52) Whitman, L. J.; Richter, L. J.; Gurney, B. A.; Villarrubia, J. S.; Ho, W. Co Adsorption Site Occupations on Fe(111) vs Coverage and Temperature: The Kinetics of Adsorption and Reaction. *J. Chem. Phys.* **1989**, *90*, 2050−2062.

(53) Sun, Y. N.; Qin, Z. H.; Lewandowski, M.; Shaikhutdinov, S.; Freund, H. J. CO Adsorption and Dissociation on Iron Oxide Supported Pt Particles. *Surf. Sci.* **2009**, *603*, 3099−3103.

(54) Parkinson, G. S.; Manz, T. A.; Novotný, Z.; Sprunger, P. T.; Kurtz, R. L.; Schmid, M.; Sholl, D. S.; Diebold, U. Antiphase Domain Boundaries at the Fe_3O_4(001) Surface. *Phys. Rev. B: Condens. Matter Mater. Phys.* **2012**, *85*, No. 195450.

(55) Beniya, A.; Higashi, S.; Ohba, N.; Jinnouchi, R.; Hirata, H.; Watanabe, Y. CO Oxidation Activity of Non-Reducible Oxide-Supported Mass-Selected Few-Atom Pt Single-Clusters. *Nat. Commun.* **2020**, *11*, No. 1888.

(56) Hulva, J.; Meier, M.; Bliem, R.; Jakub, Z.; Kraushofer, F.; Schmid, M.; Diebold, U.; Franchini, C.; Parkinson, G. S. Unraveling CO Adsorption on Model Single-Atom Catalysts. *Science* **2021**, *371*, 375−379.

(57) The intensity shown in Figure 1c is normalized to the number of Pt atoms per cluster. Taking the average cluster heights at ≥450 K from our STM measurements (see Section 3.4) into account for a conservative geometrical estimate, we can estimate the number of atoms at the rim and on the surface of the clusters and normalize them to the number of cluster atoms: Pt_5 is a single layer cluster with 5 (normalized 1) rim atoms and 5 (normalized 1) surface atoms (see Figure 4c) and Pt_{19} a bilayer cluster with ∼9 (normalized 0.5) rim and ∼16 (normalized 0.8) surface atoms, respectively. The number of active sites hence scales with the surface and not the rim of the cluster as we see similar activities per cluster atom.

(58) Szabó, A.; Henderson, M. A.; Yates, J. T. Oxidation of CO by Oxygen on a Stepped Platinum Surface: Identification of the Reaction Site. *J. Chem. Phys.* **1992**, *96*, 6191−6202.

(59) Sebetci, A. A Density Functional Study of Bare and Hydrogenated Platinum Clusters. *Chem. Phys.* **2006**, *331*, 9−18.

(60) Xiao, L.; Wang, L. Structures of Platinum Clusters: Planar or Spherical. *J. Phys. Chem. A* **2004**, *108*, 8605−8614.

(61) Yang, S. H.; Drabold, D. A.; Adams, J. B.; Ordejón, P.; Glassford, K. Density Functional Studies of Small Platinum Clusters. *J. Phys.: Condens. Matter* **1997**, *9*, L39−L45.

(62) Heredia, C. L.; Ferraresi-Curotto, V.; López, M. B. Characterization of PtN (N=2−12) Clusters through Global Reactivity Descriptors and Vibrational Spectroscopy, a Theoretical Study. *Comput. Mater. Sci.* **2012**, *53*, 18−24.

(63) Bhattacharyya, K.; Majumder, C. Growth Pattern and Bonding Trends in Ptn (n=2−13) Clusters: Theoretical Investigation Based on First Principle Calculations. *Chem. Phys. Lett.* **2007**, *446*, 374−379.

(64) Grönbeck, H.; Andreoni, W. Gold and Platinum Microclusters and Their Anions: Comparison of Structural and Electronic Properties. *Chem. Phys.* **2000**, *262*, 1−14.

(65) Sebetci, A.; Güvenç, Z. B. Energetics and Structures of Small Clusters: PtN, N = 2-21. *Surf. Sci.* **2003**, *525*, 66−84.

Supporting Information for

Cluster Catalysis with Lattice Oxygen:

Tracing Oxygen Transport from a Magnetite(001)

Support onto Small Pt Clusters

Sebastian Kaiser,[1,2] Farahnaz Maleki,[3] Ke Zhang,[1,2] Wolfgang Harbich,[4] Ueli Heiz,[1,2] Sergio Tosoni,[3] Barbara A. J. Lechner,[1,] Gianfranco Pacchioni,[3] Friedrich Esch[1,2]*

[1] Chair of Physical Chemistry, Department of Chemistry, Technical University of Munich, Lichtenbergstr. 4, 85748 Garching, Germany

[2] Catalysis Research Center, Technical University of Munich, Lichtenbergstr. 4, 85748 Garching, Germany

[3] Dipartimento di Scienza dei Materiali, University of Milano-Bicocca, via Roberto Cozzi 55, 20125 Milano, Italy

[4] Institute of Physics, Ecole Polytechnique Fédérale de Lausanne, CH-1015 Lausanne, Switzerland

* bajlechner@tum.de

1

S1. Pulsed reactivity data evaluation
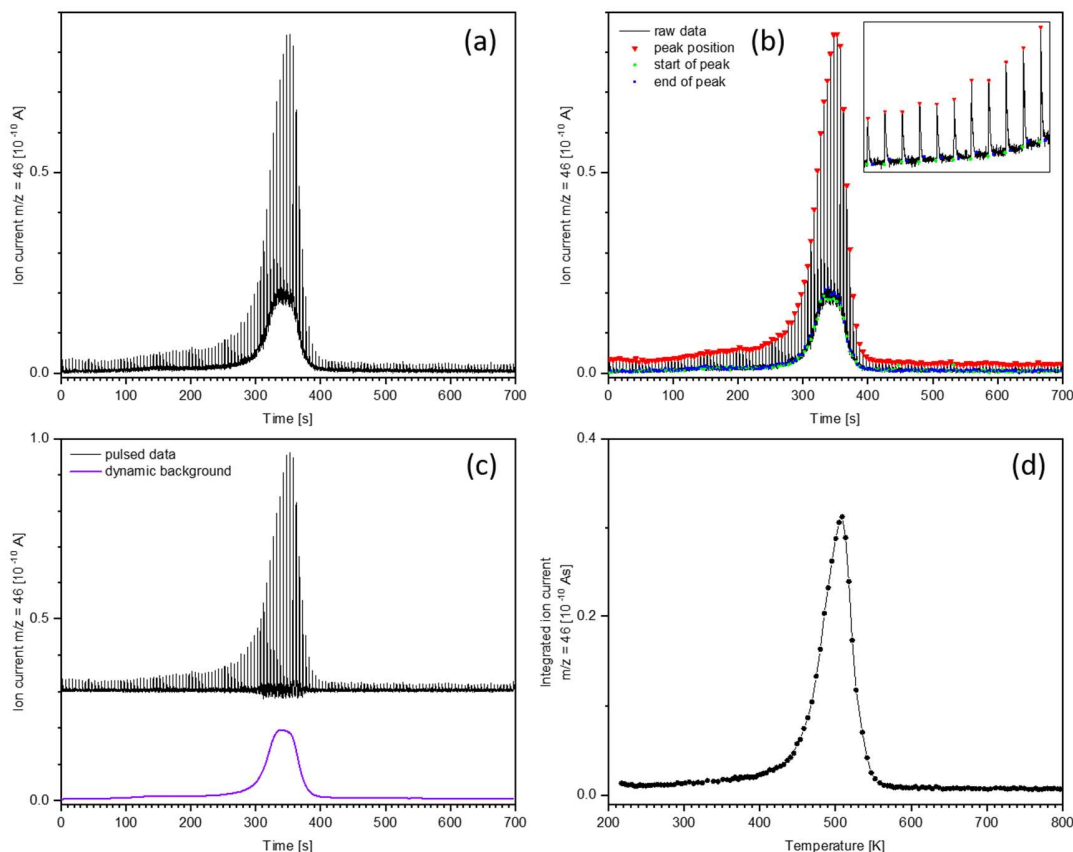
Figure S1. Evaluation procedure for pulsed valve sniffer measurements. (a) displays the measured raw data, consisting of a series of pulses convoluted with a continuous dynamic background (usually caused by desorption or reaction products). As both components contain information about the investigated system, it is necessary to separate them. First, the peak position (red), as well as the start (green) and end (blue) of each peak are detected, as shown in (b). The inset shows a zoomed-in section to better illustrate the method. The data in between the pulses (determined by the start and end points of the pulses) is smoothed and interpolated to determine the dynamic background, which is then subtracted. (c) shows the pulsed data after background subtraction (black, with an offset of 3×10^{-11} A), as well as the subtracted background (purple). Finally, each individual pulse is integrated numerically and the resulting values are plotted vs. temperature, as shown in (d).

S2. Characterization of magnetite bulk and (001) surface by DFT calculations

We started from the experimental crystal structure of Fe_3O_4 using a supercell with a $Fe_{24}O_{32}$ ($(Fe_3O_4)_8$) formula. Fe_3O_4 (magnetite) has the structure of a cubic inverse spinel with Fe^{3+} in the tetrahedral sites and a 50:50 mixture of Fe^{2+} and Fe^{3+} in the octahedral sites.[1] Tetrahedral and octahedral sublattices are anti-ferrimagnetically aligned in Fe_3O_4, such that the magnetic moments of the Fe^{3+} cations on each sublattice cancel each other, and a nominal net magnetization of 4 μ_B per Fe_3O_4 formula unit derives from the Fe^{2+} cations. We first optimized the lattice and internal coordinates with PBE+U+D3. The calculated lattice parameters (Table S1) show a slight distortion from the cubic symmetry. The lattice volume is overestimated by 2%, indicating a reasonable agreement of the hereby adopted computational method with the experiment.

Table S1. Calculated and experimental lattice parameters (a, b and c, Å) and cell volume ($Å^3$) of cubic Fe_3O_4.

	Calc.	Exp.[a]
a	8.451	8.397
b	8.458	8.397
c	8.458	8.397
Cell Volume	604.59	592.1

[a] Data from ref [2]

The calculated electronic structure displays 4 unpaired electrons per formula unit, as reported in experiments (32 unpaired electrons in the unit cell). Figure S2 shows the spin density iso-surface of magnetite. Fe atoms in tetrahedral positions (Fe^{3+}) are spin down while the Fe atoms in octahedral sites are spin up (half Fe^{3+} and half Fe^{2+}), consistent with an anti-ferrimagnetic ordering. In agreement with previous reports adopting a similar level of theory, magnetite is a semimetal, displaying conducting character on one spin channel and a small band gap (≈ 0.5 eV) on the other.
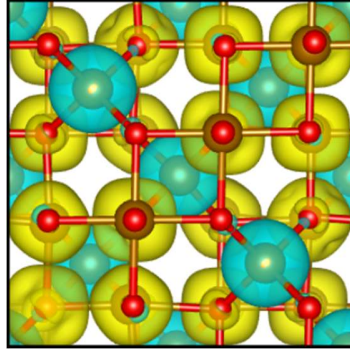
Figure S2. Spin-density iso-surface (0.01 $|e|/\text{Å}^3$) of bulk Fe_3O_4, with α (spin-up) electrons density in yellow and β (spin-down) in cyan.

The magnetite(001) surface is modelled following the sub-surface cation vacancy structure proposed by Parkinson.[3] The 1×1 cell's content is $Fe_{35}O_{48}$, where one Fe ion in an octahedral site of the subsurface layer has been removed. The hereby adopted slab model contains 12 atomic layers; the ions from the bottom 4 layers are kept frozen in their bulk lattice position, and all others are relaxed. As previously observed,[1] one Fe atom in the second atomic layer moves during the relaxation from an octahedral to a tetrahedral site, Figure S3. There are thus 13 Fe atoms in tetrahedral and 22 Fe atoms in octahedral positions. The total number of unpaired electrons in the supercell is 40 (3.3 per formula unit, showing a remarkable quenching of the magnetic moment with respect to the bulk).
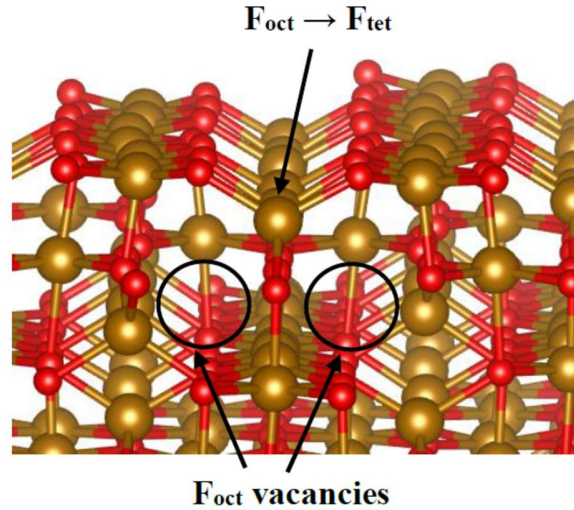
Figure S3. Optimized structure of the subsurface cation vacancy model of Fe_3O_4(001).

S3. Formation of a surface oxygen vacancy on various sites

In this section, we describe the effect of generating an oxygen vacancy on the surface of magnetite. Given the focus of the present paper on the surface properties of magnetite, we did not consider the vacancy formation in the subsurface and bulk regions. As shown in Figure S4, there are three non-equivalent O atoms on the first atomic layer of the $Fe_3O_4(001)$ slab: O1 and O2 are next to an iron atom in a tetrahedral site and O3 is above an iron atom in an octahedral site (Figure S4). The formation energy of an oxygen vacancy (E_f), Table S2, is calculated as follows:

$$E_f = E[Fe_3O_{4-x}] + E[\tfrac{1}{2} O_2] - E[Fe_3O_4] \quad\quad\quad (1)$$

$$E'_f = E[Fe_3O_{4-x}] + E[O] - E[Fe_3O_4] \quad\quad\quad (2)$$

The O3 vacancy has the lowest formation energy of 2.91 eV; the other oxygens are removed at a somewhat higher cost, as shown in Table S2. Notably, the formation of a vacancy in O3 increases the net magnetization per formula unit from 3.4 μ_B (pristine surface) to 3.8 μ_B, while the removal of O1 or O2 species has little effect on the magnetization.

Table S2. Formation energy of an oxygen vacancy (E_f computed with respect to $\tfrac{1}{2} O_2$ and E'_f computed with respect to atomic O, in eV) and magnetic moment per unit cell (M_{total}, μ_B) on the (001) surface of Fe_3O_4, illustrated in Figure S4.

	E_f	E'_f	M_{total}
V_{O1}	3.55	6.93	3.34
V_{O2}	3.10	6.48	3.32
V_{O3}	2.91	6.30	3.79
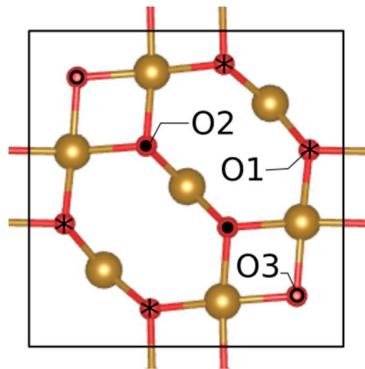
Figure S4. Top view of the first and second atomic layers of the $Fe_3O_4(001)$ unit cell. O1, O2 and O3 indicate the non-equivalent O atoms on the surface of the $Fe_3O_4(001)$ slab.

S4. CO desorption from bare magnetite and magnetite-supported clusters in TPD
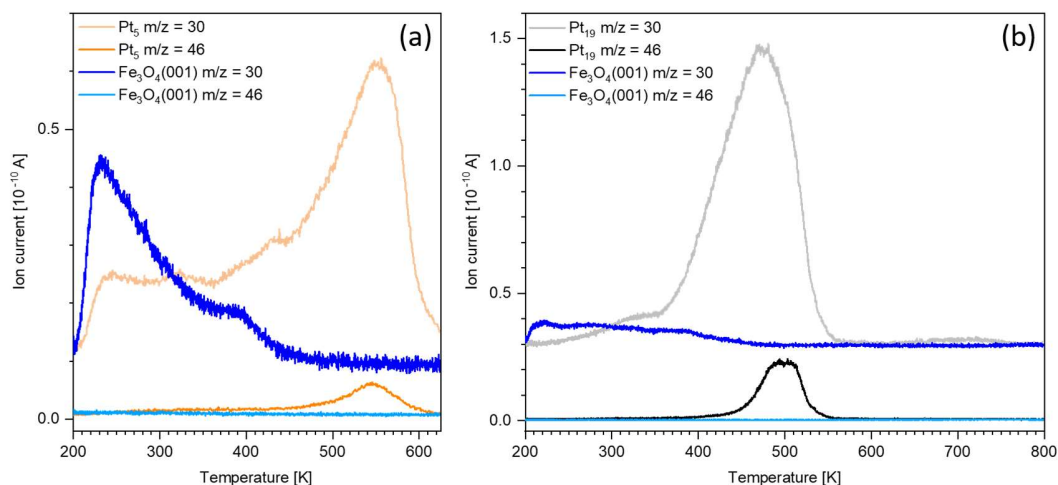
Figure S5. Saturation $C^{18}O$ TPD curves of (a) Pt5 (orange) and (b) Pt19 (gray) supported on $Fe_3O_4(001)$ compared to the corresponding desorption curves from the clean support (blue). The heating rate was 1 K/s. The $C^{18}O$ (m/z = 30) and $C^{18}O^{16}O$ (m/z = 46) signals are shown. The clean magnetite surface exhibits several overlapping, not very distinct CO desorption features in the temperature region investigated here. The desorption starts immediately upon heating and is finished below 450 K. These background desorption features are the high temperature shoulder of a much larger desorption peak located around 180 K, which is attributed to an unidentified magnetite surface defect.[4] It can be observed that especially the beginning of the background CO desorption around 230 K is much less pronounced with clusters deposited on the $Fe_3O_4(001)$ surface, indicating that a part of the defects are no longer accessible CO adsorption sites. This effect can be explained by at least some of the clusters occupying surface defect sites. Furthermore, it is shown that no CO_2 desorption or production from the bare $Fe_3O_4(001)$ surface is detectable in the measured temperature region (cyan).

S5. Ripening of Pt₅ in STM
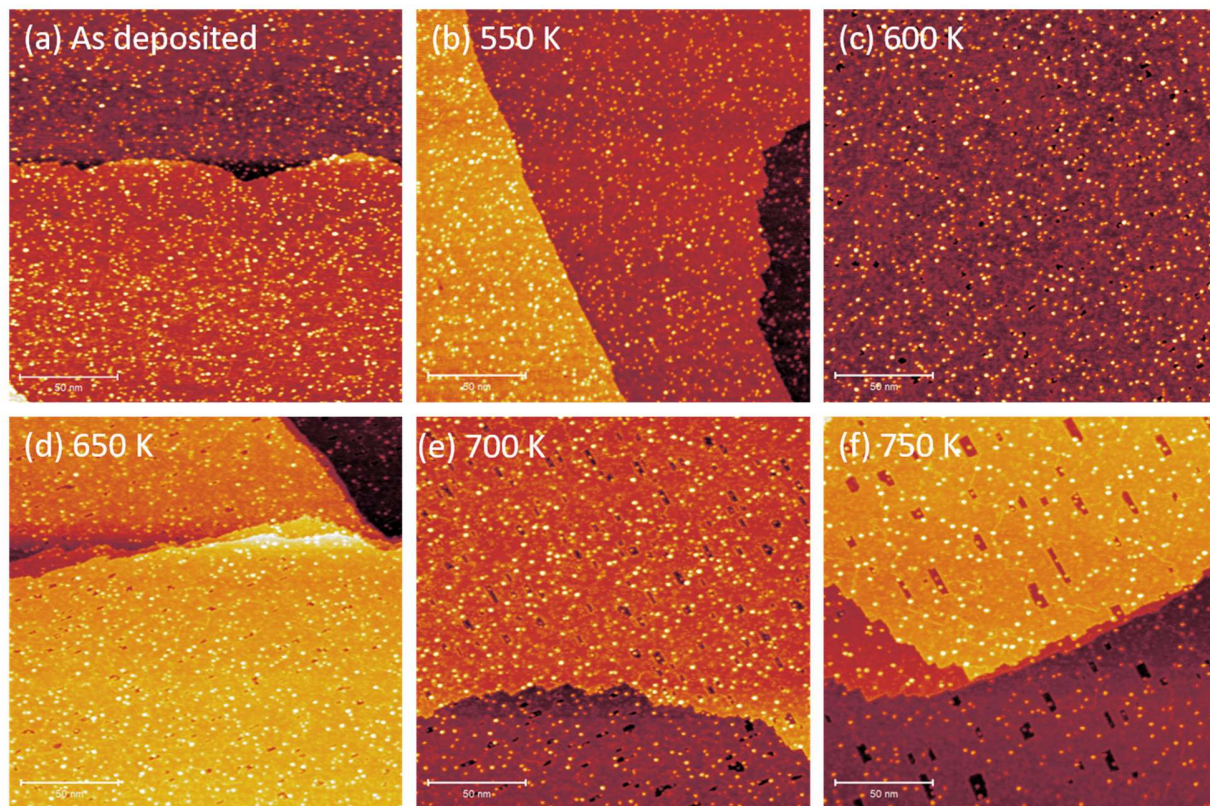
Figure S6. STM image series of Pt$_5$ clusters (0.05 clusters/nm^2) on Fe$_3$O$_4$(001), (a) as deposited at RT, (b-f) measured at RT after annealing to the temperatures indicated, respectively. Up to an annealing temperature of 600 K, the number of clusters stays constant. Above 650 K, gradual cluster ripening is observed, yielding fewer clusters with an average size of about Pt$_{15-20}$ at 750 K. The approximate size is calculated by comparing the apparent height and number of clusters at 750 K with the as-deposited sample. Upon annealing, hole formation in the periphery of some clusters is observed, due to lattice oxygen migrating onto the clusters and reaction with background CO, while the residual, reduced iron atoms diffuse into the bulk. *Imaging parameters: V$_b$ = 1.50 V; I$_t$ = 300 pA.*

S6. Alternating CO and O_2 pulses on Pt_5/Fe_3O_4(001)
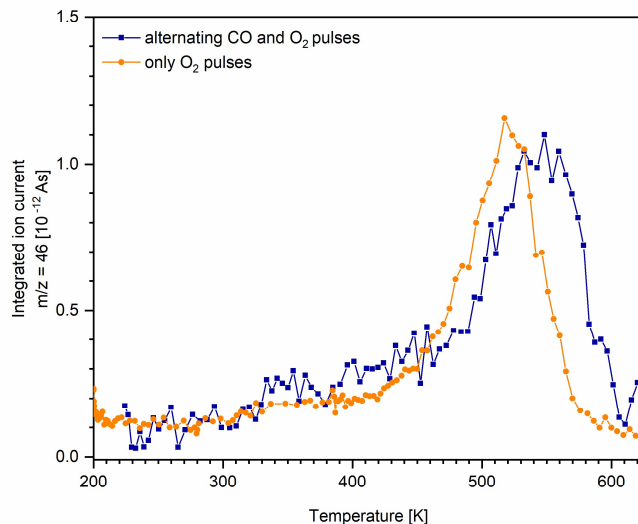
Figure S7. CO_2 production synchronized with O_2 pulses as a function of temperature, obtained by pulsing only O_2 (orange) and alternatingly pulsing CO and O_2 (blue) on CO pre-covered Pt_5 clusters on Fe_3O_4(001). Both curves have been normalized to the number of Pt atoms per cluster. When additionally pulsing CO, the onset of the CO_2 production peak synchronized with O_2 pulses is shifted to higher temperatures, indicating a stronger initial poisoning of the cluster surface by CO since the CO pulses shift the desorption equilibrium. The peak position is similarly shifted from 520 K to 550 K. This indicates a reaction limitation due to a lack of CO when only pulsing O_2.

S7. Loss of CO adsorption capability upon cluster encapsulation
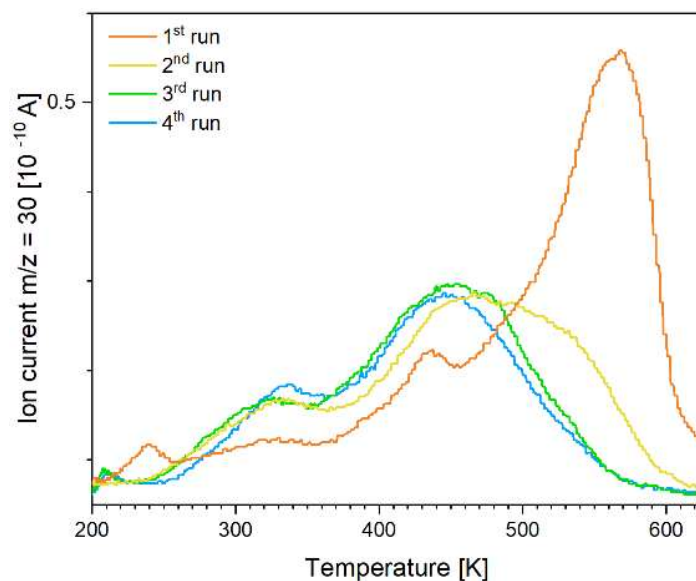
Figure S8. Subsequent saturation $C^{18}O$ TPD curves (m/z = 30) of Pt$_5$ clusters (0.05 clusters/nm^2) on Fe$_3$O$_4$(001), corresponding to the TPD experiments shown in Figure 2. For every run, the surface was saturated with $C^{18}O$ at 200 K, the heating rate was 1 K/s. The main peak in the first run (orange) at 550 K is attributed to the clusters. Several lower temperature features are observed as well, which most certainly are related to surface defects (as described in section 3.1 in the main text). In the second run (yellow) the cluster-related desorption feature decreases significantly, while two broad lower temperature peaks arise at 325 K and 450 K. In the third TPD run (green), the CO desorption from the cluster vanishes almost completely, while the lower temperature peaks become slightly more pronounced. In the fourth run (blue), only the lower temperature peaks occur. This subsequent decrease in CO adsorption capability of the clusters is attributed to encapsulation as a result of SMSI, comparable to Pt nanoparticles supported on Fe$_3$O$_4$(001) that become encapsulated by an FeO layer upon annealing.[5] The TPD series indicates that after the first run, the clusters are partially encapsulated, with still a fraction of their surface accessible for CO adsorption. In the following runs, the clusters become completely encapsulated, thus no cluster-related CO desorption is observed anymore. The lower temperature features appear simultaneously with the encapsulation of the clusters and may therefore originate from CO desorption from the encapsulating layer, which is expected to be non-stoichiometric reduced iron oxide, since the lower temperature peaks are well within the temperature range of CO desorption from FeO surfaces.[6] However, more experiments have to be done for further clarification.

S8. Hole formation in cluster periphery
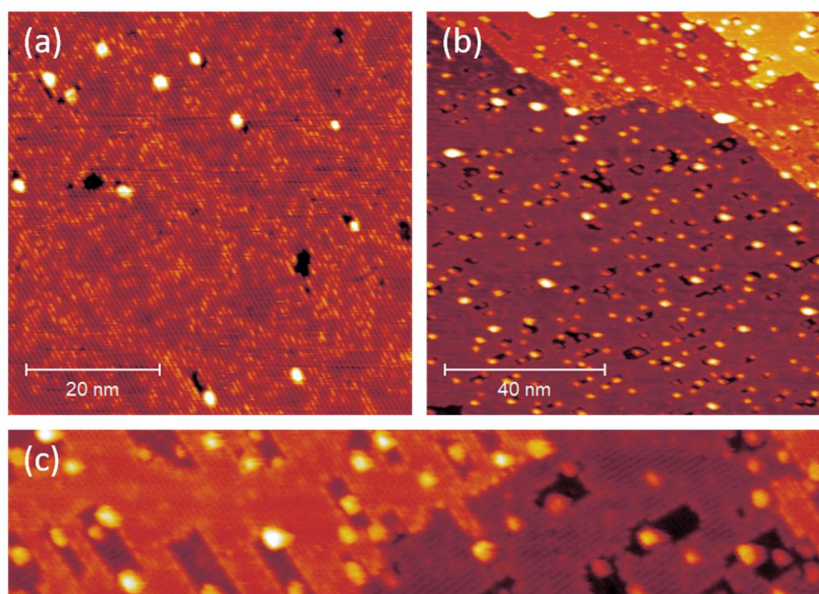
Figure S9. Hole formation around Pt clusters on Fe_3O_4(001). (a) shows Pt_{10} clusters (0.01 clusters/nm^2) measured at 573 K. Clear hole formation in the cluster periphery can be observed caused by the removal of lattice oxygen around the clusters by reverse spillover and reaction with CO from the chamber background, followed by Fe migration into the bulk. (b) and (c) display Pt_{19} (0.05 clusters/nm^2) measured at RT after annealing to 590 K in 1 x 10^{-7} mbar CO for 2 minutes. Again, hole formation around the clusters can be observed, but much more pronounced compared to samples annealed in UHV as a consequence of the higher CO partial pressure. The holes exhibit a rectangular shape which changes direction between two neighboring terraces, following the direction of the atomic rows of the support. This becomes very obvious in the zoomed-in area in (c). The holes are fairly large compared to the clusters, indicating a facile oxygen diffusion towards the clusters at elevated temperatures. The edges of the holes are straight and terminated by an iron row of the magnetite lattice, but more rough perpendicular to them. This indicates that the oxygen diffusion is more favorable along an atomic row, suggesting the initial removal of an oxygen atom from a pristine atomic row to be most difficult. *Imaging parameters:* V_b = 1.50 V; (a) I_t = 500 pA, (b, c) I_t = 300 pA.

S9. Platinum clusters in the gas phase: structure relaxation and oxygen adsorption

The minimum energy structures of gas phase Pt clusters have been studied in previous DFT investigations.[7–13] For instance, the calculations with a B3PW91 hybrid functional show that a Pt_5 cluster with distorted squared pyramid geometry, Figure S10(iii), is the lowest energy isomer.[7] Here, we have considered six of the most stable isomers, and recomputed their stabilities and structures at the PBE+U+D3 level, Figure S10. Four isomers are within an energy of 200 meV, and all six isomers are within 0.35 eV, with energy differences of 70-80 meV, respectively. This suggests a high fluxionality in the gas phase. Of course, once deposited on an oxide support, the structural flexibility of the Pt clusters could be reduced.
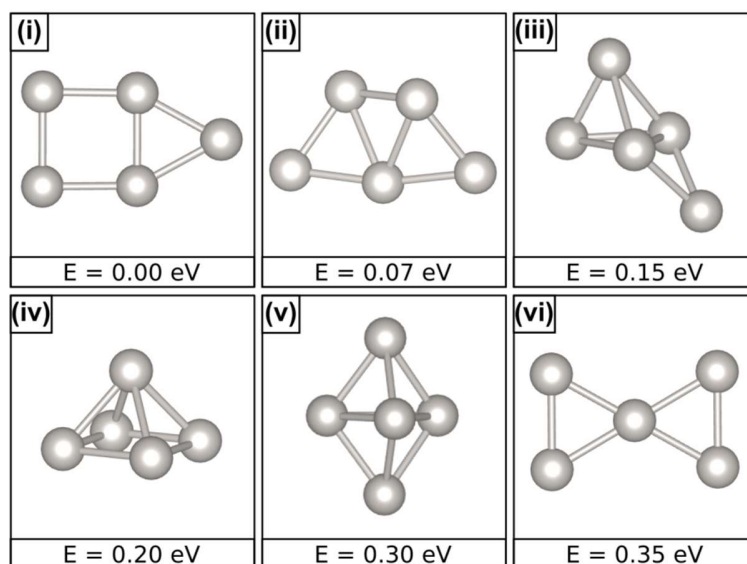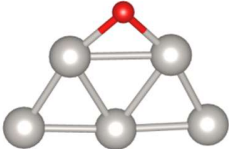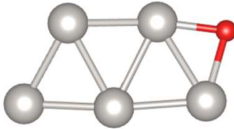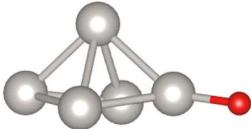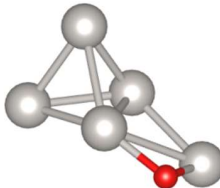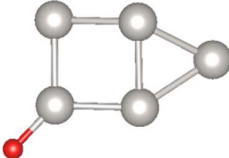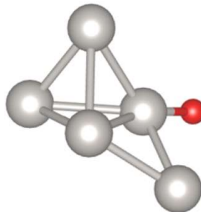
Figure S10. Optimized structures and relative energies of isomers of the Pt_5 gas phase cluster.
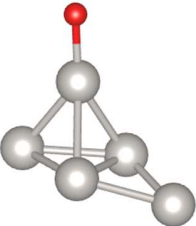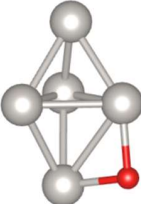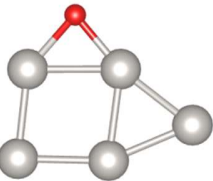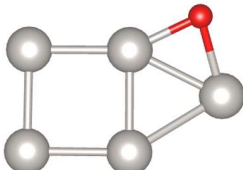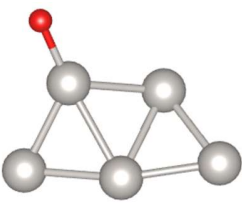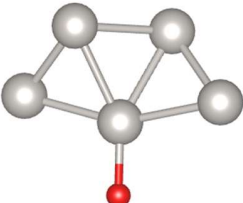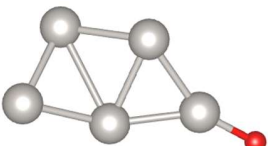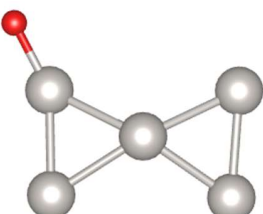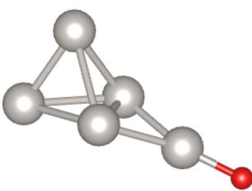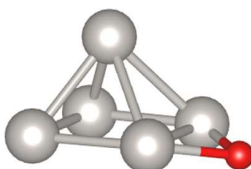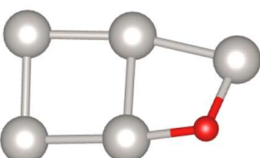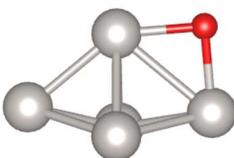
We consider the preferred adsorption sites for a single O atom on the various isomers of gas phase Pt_5. Altogether, we have considered 25 possible structures, and this is not necessarily an exhaustive sample. The adsorption of an O atom on the (i) to (vi) Pt_5 clusters, summarized in Table S3, occurs in three positions: terminal, bridge and hollow. In many cases, the position of the adsorbed O atom and/or the shape of cluster change during optimization. Table S3 reports the optimized structures, their relative energy (E_R), and the adsorption energy (E_{ADS}) of an O atom with respect to the most stable Pt_5 (i) cluster and ½ O_2 molecule, calculated as follows:
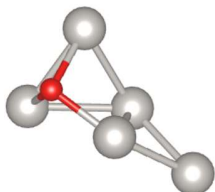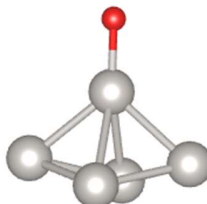
$$Pt_5(i) + \tfrac{1}{2} O_2 \rightarrow O\text{-}Pt_5(n) \qquad \Delta E = E_{ADS} \qquad\qquad (3)$$
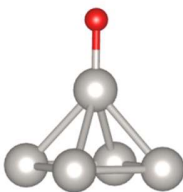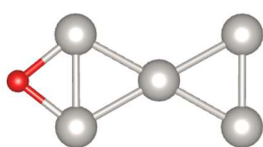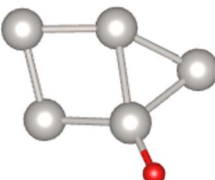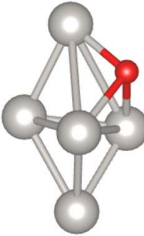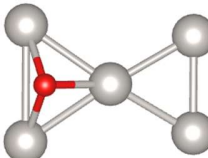
The most stable gas phase Pt_5O cluster is planar, with the Pt atoms forming three fused triangles and the O atom adsorbed in a Pt-Pt bridge position. The next most stable isomer has a completely different structure: it is three-dimensional with the adsorbed O in a terminal position, bound to an apical Pt atom. It is 0.42 eV higher in energy than the ground state structure. Also the next two stable isomers 3 and 4, Table S3, show the presence of O in a terminal position. In general, an O atom binds preferentially in a Pt-Pt bridge site only if the Pt-Pt distance is such to favour its coordination. Cases where the O atom is in a hollow site are clearly higher in energy.

Table S3. Relative energy (E_R, eV) and adsorption energy (E_{ADS}, eV) of an adsorbed O atom on Pt_5 clusters.

Structure		E_R	E_{ADS}	Structure		E_R	E_{ADS}
1		0.00	-2.42	13		0.95	-1.47
2		0.42	-2.00	14		0.98	-1.44
3		0.53	-1.89	15		1.09	-1.33

4		0.63	-1.80	16		1.11	-1.31

5		0.65	-1.78	17		1.16	-1.27

6		0.67	-1.75	18		1.18	-1.24

7		0.67	-1.75	19		1.21	-1.21

8		0.77	-1.65	20		1.26	-1.17

9		0.83	-1.60	21		1.30	-1.12

10		0.83	-1.59	22		2.11	-0.31
11		0.86	-1.56	23		2.12	-0.30
12		0.91	-1.52	24		2.18	-0.24
				25		2.22	-0.20

S10. Adsorption of Pt_5 on $Fe_3O_4(001)$ and formation of oxygen vacancies

Table S4. Adsorption energy (E_{ADS}, eV), Bader charge (q, $|e|$), and spin polarization of adsorbed Pt_5 clusters on Fe_3O_4 and total spin magnetic moment per unit cell (M_{total}, μ_B).

Figure	$E_{ADS}^{(a)}$	$q(Pt_5)$	$M(Pt_5)$	M_{total}
4(a)	-4.51	0.33	0.08	2.59
4(b)	-3.01	0.25	1.12	3.17
4(c)	-2.73	0.33	0.19	3.22

[a] Energy change related to the reaction $Pt_5(i) + Fe_3O_4 \rightarrow Pt_5(n)/Fe_3O_4$

The Pt_5 adsorption energies, reported in Table S4, are calculated with respect to the clean support and the gas phase cluster in its most stable configuration (capped square, Figure S10(i)).

The formation energy of the oxygen vacancy (E_f), Table S5, has been calculated according to the following equation:

$$E_f = E[(Pt_5/Fe_3O_{4-x})] + E[\tfrac{1}{2} O_2] - E[(Pt_5/Fe_3O_4)] \tag{4}$$

Table S5. O vacancy energy (E_f, eV), Bader charge (q, $|e|$), spin polarization of an adsorbed Pt_5 cluster (Figure 4(a)) and total spin magnetic moment per unit cell (M, μ_B). The position of the O atom removed is shown in the Figure.

	E_f	$q(Pt_5)$	$M(Pt_5)$	M_{total}
V_{O1}	3.14	-0.27	0.20	2.61
V_{O2}	1.98	-0.37	0.27	3.24
V_{O3}	2.66	-0.50	0.28	2.49
V_{O4}	2.46	0.24	0.35	3.40

As discussed in the main text, we observe a general decrease in the formation energy in the presence of the platinum clusters with respect to the clean support. The reduction of the substrate upon oxygen removal, however, does not imply a remarkable charge transfer to the cluster, as shown by the Bader charges. In some cases, in particular V_{O1} and V_{O3}, a significant decrease of the net magnetization is reported.

S11. Lattice oxygen reverse spillover

(i)   Displacement of one oxygen atom

The study of the formation of an O vacancy on the clean support has shown that O2 is the easiest O to remove, as shown in Table S5. In this section, we consider the energetic cost of displacing the O2 atom from the support and adsorbing it on a Pt_5 cluster. The process corresponds to the final state of a lattice oxygen reverse spillover effect. The O atom has been re-adsorbed on various sites of the supported Pt_5 cluster, always starting from the most stable structure, Figure 4(a) in the main text, corresponding to the Pt_5(iii) gas phase isomer. Other structures have also been considered, some of them being unstable. For instance, O adsorption on one of the triangular facets of Pt_5 always resulted in an O atom bound to a bridge site. The most stable isomers found are shown in Figure S11 in order of stability (see also Table S6).
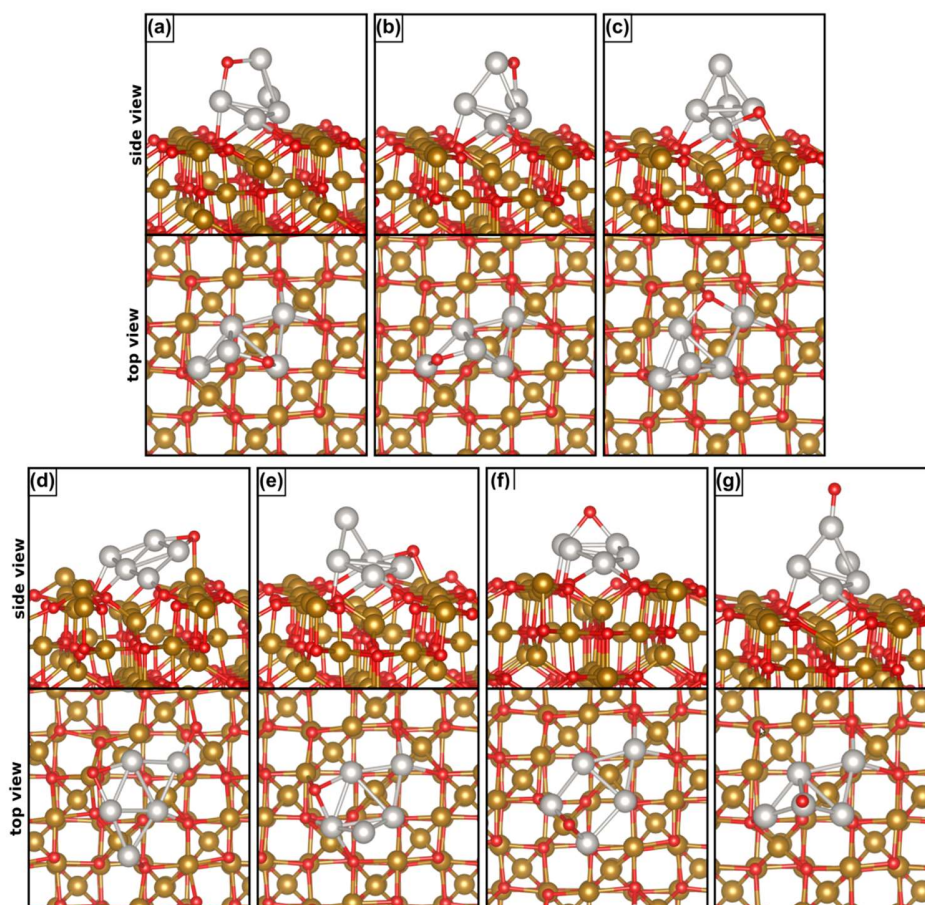
Figure S11. Various isomers of Pt_5O supported on Fe_3O_4. The structures have been obtained starting the geometry optimization from Pt_5/Fe_3O_4, Figure 4(a).

The most stable structure is that of a capped rhombus Pt_5 with an O atom adsorbed on one bridge site, shown in Figure S11(a). The corresponding energy is -0.40 eV lower than that of Pt_5/Fe_3O_5 (see Table S6).

Table S6. O reverse spillover energy (E_{SO}, eV), Bader charge (q, $|e|$), spin polarization of $Pt_5/Fe_3O_4(001)$ and the total spin magnetic moment per unit cell (M_{total}, μ_B).

Figure	$E_{SO}^{(a)}$	$q(Pt_5)$	$q(O_{spill})$	$M(Pt_5)$	M_{total}
S11 (a)	-0.40	0.25	-0.68	0.03	3.26
S11 (b)	-0.15	0.29	-0.68	0.70	3.32
S11 (c)	-0.04	0.67	-0.86	0.48	3.27
S11 (d)	0.40	0.14	-0.82	0.98	3.80
S11 (e)	0.74	0.27	-0.81	0.08	4.51
S11 (f)	0.86	0.40	-0.72	0.07	3.92
S11 (g)	1.68	0.22	-0.57	0.13	3.46

(a) E_{SO} refers to the energy of this reaction: $Pt_5/Fe_3O_4 \rightarrow O\text{-}Pt_5/Fe_3O_{4-x}$

This shows that the lattice oxygen reverse spillover in this specific case is an exothermic process. A second isomer, Figure S11(b), is only 0.25 eV higher in energy and differs from the isomer of Figure S11(a) only for the Pt-Pt bond that is bridge-bonded by O. A third interesting structure is shown in Figure S11(c). Here, the O atom is bridging a Pt-Pt bond at the cluster/oxide interface. It can be considered the first step in the migration of an O atom from the support onto the cluster. The isomer shown in Figure S11(c) is -0.04 eV lower in energy than the starting structure, i.e. is thermoneutral with respect to the case where no O vacancy has been formed on the support, and no oxygen has been transferred to Pt_5. Other Pt_5O isomers are shown in Figure S11(d)-(g); they are all higher in energy than the three best structures shown in Figure S11(a)-(c).

(ii)   Displacement of two oxygen atoms

Next, we have considered the spillover of two oxygen atoms from the magnetite surface onto Pt_5. Different O atoms have been removed from the support, and different adsorption positions have been considered on Pt_5O, starting from the most stable structures obtained for the case of a single O reverse spillover, as shown Figure S11. The results are reported in Figure S12 and Table S7.
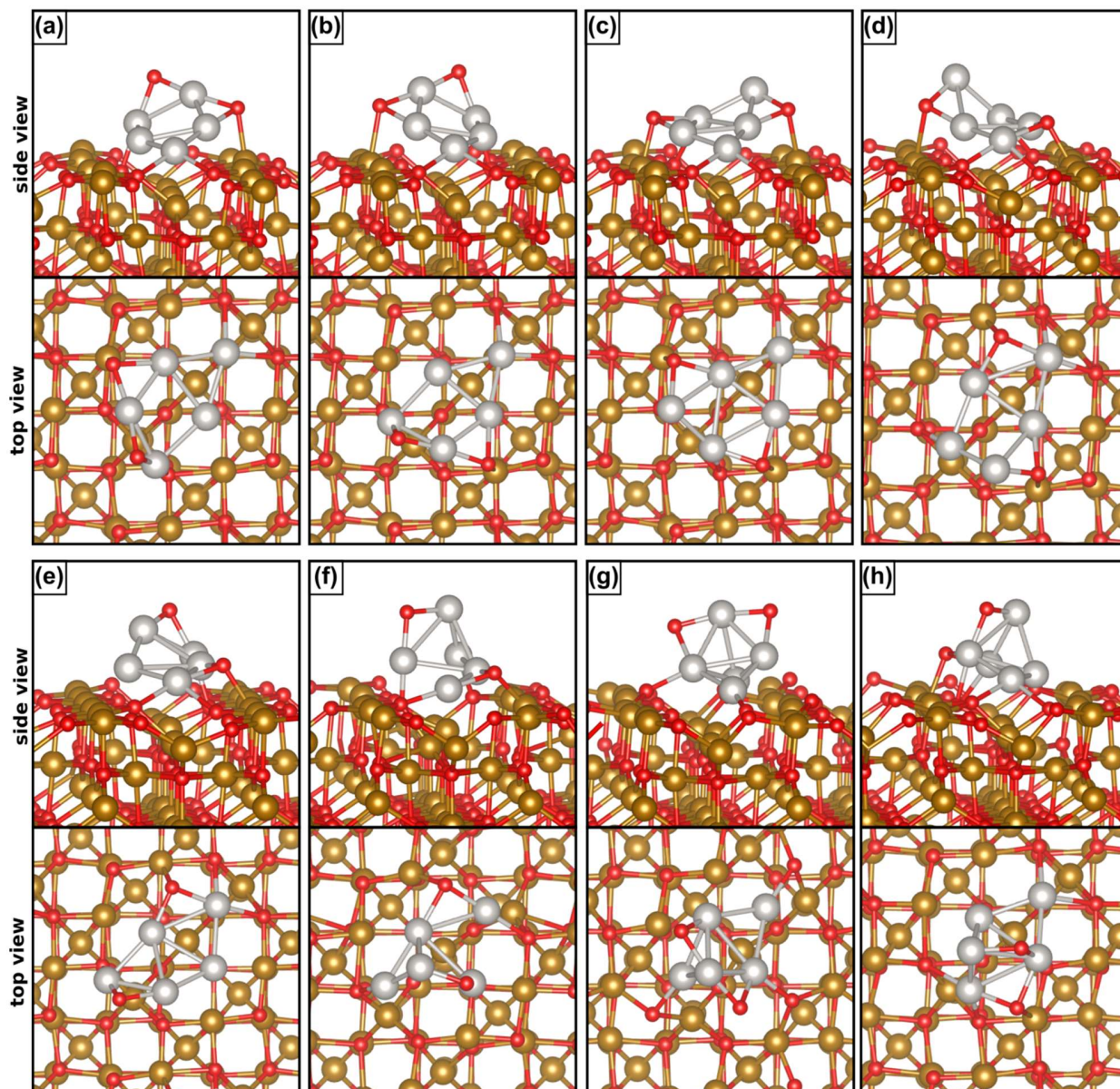
Figure S12. Various isomers of Pt$_5$O$_2$ supported on Fe$_3$O$_{4-x}$. The structures have been obtained starting the geometry optimization from Pt$_5$O/Fe$_3$O$_{4-x}$, Figure 5(a). (a) to (d) O2 and O4 spillover; (e) O1 and O2 spillover; (g) and (h) O2 and O4 spillover (see Table S5).

We found two isomers, shown in Figure S12(a) and (b) whose structures are *lower* in energy, by -0.64 and by -0.56 eV, Table S7, than the regular, non-defective surface with adsorbed Pt$_5$. This is an important result which shows that multiple oxygen transfer from the support to a small Pt cluster is thermodynamically favorable, and by a considerable amount. These two structures have been obtained by removing the O2 and O4 atoms of the surface, in the periphery of the Pt$_5$ cluster, as

shown in Figure 5(b) in the main text. An important observation is that after geometry optimization, the Pt_5O_2 cluster changes its structure and from 3D (Figure S11(a)) it becomes nearly flat, as shown in Figure S12(a) and (b).

Pt_5 structures that maintain the original 3D shape, a capped rhombus (Figures S11(f) and (g)), are slightly below or slightly above the Pt_5/Fe_3O_4 reference, but clearly higher in energy than the nearly 2D ground state structures.

These results show two important trends: (1) multiple lattice oxygen reverse spillover is an energetically favorable process; and (2) the adsorption of two oxygen atoms on Pt_5 leads to a restructuring that tends to flattens the cluster structure. In order to confirm these trends, in the next Section we considered the spillover of three oxygen atoms.

Table S7. Oxygen spillover energy (E_{SO}, eV), Bader charge (q, |e|), spin polarization of $Pt_5/Fe_3O_4(001)$ and the total spin magnetic moment per unit cell (M, μ_B).

	Figure	$E_{SO}^{(a)}$	$q(Pt_5)$	$q(2O_{spill})$	$M(Pt_5)$	M_{total}
O2, O4	S12 (a)	-0.64	0.37	-1.52	0.21	2.54
	S12 (b)	-0.56	0.48	-1.50	0.15	3.92
	S12 (c)	0.59	0.41	-1.62	0.19	3.96
	S12 (d)	0.83	0.46	-1.61	0.19	3.93
	S12 (e)	0.86	0.49	-1.52	0.56	2.54
O1, O2	S12 (f)	0.30	0.53	-1.58	0.65	3.34
O2, O4	S12 (g)	-0.04	0.73	-1.40	0.35	3.18
	S12 (h)	1.66	1.07	-1.46	0.40	3.99

(a) E_{SO} refers to the process: $Pt_5/Fe_3O_4 \rightarrow 2O\text{-}Pt_5/Fe_3O_{4-x}$

(iii)   *Displacement of three oxygen atoms*

We finally considered the case where three oxygen atoms are displaced from the magnetite surface onto the Pt_5 cluster, with formation of a Pt_5O_3 unit and three oxygen vacancies. The number of potential isomers is huge, and we restricted the analysis to the sites where oxygen is easier to remove, O1, O2, and O4 or O1, O2 and O5, and to a few structures derived from the best isomers of Pt_5O_2, as shown in Figure S13 and Table S8. The two most stable structures are shown in Figure S13 (a) and (b) and correspond to a flat or nearly flat Pt_5 with three oxygen atoms in bridge sites; some of them remain at the cluster/support interface and thus coordinated to Fe atoms of the support, providing anchoring points for the nanocluster. These two structures are only 0.17 and 0.23 eV higher in energy, respectively, than the pristine Pt_5/Fe_3O_4, showing that even the transfer

of three oxygen atoms is energetically possible (the reaction is only slightly endothermic). We cannot exclude that some more favorable isomers exist, but this already provides sufficient evidence that multiple oxygen transfer from magnetite to supported Pt clusters is possible.
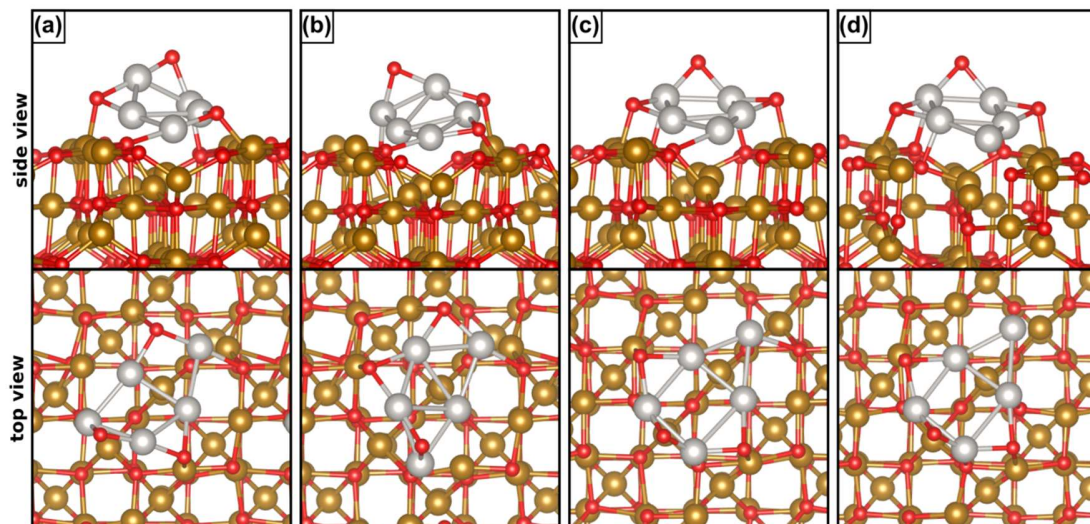

Figure S13. Various isomers of Pt_5O_3 supported on Fe_3O_{4-x}. The structures have been obtained starting the geometry optimization from Pt_5O_2/Fe_3O_{4-x}, (a) to (c) O1, O2 and O4 spillover; (d) O1, O2 and O5 spillover (see Table S5).

Table S8. Three O spillover energy (E_{SO}, eV), Bader charge (q, $|e|$), spin polarization of $Pt_5/Fe_3O_4(001)$ and the total spin magnetic moment per unit cell (M, μ_B).

Figure	E_{SO}[a]	$q(Pt_5)$	$q(3O_{spill})$	M (Pt_5)	M_{total}
S13 (a)	0.17	0.85	-2.43	0.31	3.16
S13 (b)	0.23	1.00	-2.48	0.10	4.58
S13 (c)	0.95	0.71	-2.35	0.79	2.57
S13 (d)	3.85	0.93	-2.68	0.11	3.33

[a] E_{SO} refers to the process: $Pt_5/Fe_3O_4 \rightarrow 3O\text{-}Pt_5/Fe_3O_{4-x}$

20
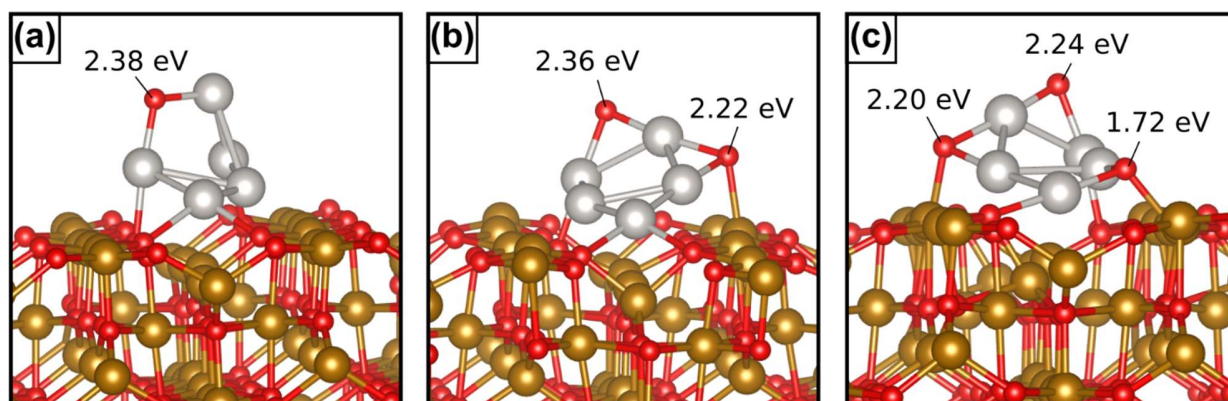
Figure S14. Energy (in eV) required to remove O atoms bound on top of Pt_5 or at the rim, i.e. at the interface between Pt_5 and Fe_3O_{4-x}.

S12. Impact of lattice oxygen reverse spillover on cluster height

In Table S9 we provide some evidence that the lattice oxygen reverse spillover mechanism, with formation of Pt_xO_y clusters, can contribute to a structural change and in particular to a transition from 3D to 2D. For all the structures considered, we have computed the average vertical distance of the Pt atoms from the surface of magnetite. Since the atoms of the surface may be involved in structural changes, we have taken the vertical distance of the Pt atoms from the bottom layer of our slab, whose coordinates are fixed. The most stable Pt_5 cluster, shown in Figure 4 (a) in the main text, is taken as a reference. We define ΔZ as the difference of the average distance of the Pt atoms in the various oxidized clusters (see Figures S11-S13).

The most stable Pt_5O cluster (see Figure S11 (a)), exhibits $\Delta Z = -0.102$ Å; the most stable Pt_5O_2 cluster (see Figure S12 (a)) has $\Delta Z = -0.386$ Å; and the most stable Pt_5O_3 cluster (see Figure S13 (a)) has $\Delta Z = -0.426$ Å. This trend is not fortuitous and is found also for the other most stable Pt_xO_y clusters, as shown in Table S9. The physical reason for this is that some of the O atoms bind at the cluster rim, and interact also with Fe ions on the surface. In order to increase this bonding, the cluster flattens its structure, resulting in a transition from 3D to 2D.

Table S9. Different distances of Pt_5O_x clusters to the magnetite support with respect to Pt_5/Fe_3O_4.

	Figures	Z_{avg}(Å)	ΔZ(Å)
Pt_5/Fe_3O_4	**4 (a)**	**13.734**	**0.000**
	4 (b)	13.908	0.174
	4 (c)	13.424	-0.310
One O spillover	S11 (a)	13.632	-0.102
	S11 (b)	13.662	-0.072
	S11 (c)	13.735	0.001
	S11 (d)	13.478	-0.256
	S11 (e)	13.419	-0.315
	S11 (f)	13.245	-0.489
	S11 (g)	13.631	-0.103
Two O spillover	S12 (a)	13.348	-0.386
	S12 (b)	13.344	-0.390
	S12 (c)	13.408	-0.326

	S12 (d)	13.414	-0.320
	S12 (e)	13.284	-0.450
	S12 (f)	13.547	-0.187
	S12 (g)	13.512	-0.222
	S12 (h)	13.478	-0.256
Three O spillover	S13 (a)	13.308	-0.426
	S13 (b)	13.435	-0.299
	S13 (c)	13.172	-0.562
	S13 (d)	13.312	-0.062

$Z_{avg} = \Sigma\ z(Fe,O)$ bottom layer$/m - \Sigma\ z(Pt)$ cluster$/n$

$\Delta Z = Z_{avg}(Pt_xO_y) - Z_{avg}(Pt_5)$

S13. Iron spillover

There are two kinds of non-equivalent Fe atoms on the first and second atomic layers of the $Fe_3O_4(001)$ slab: Fe atoms in the octahedral and tetrahedral positions, respectively, as shown in Figure S15. The formation energy of a Fe vacancy (E_f), listed in Table S10, is calculated according to the following equations:

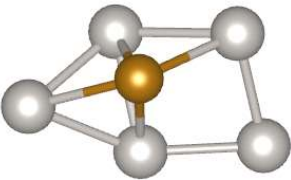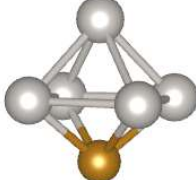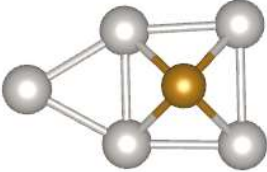$$E_f = E[Fe_{3-x}O_4] + E[Fe\ (s)] - E[Fe_3O_4] \tag{5}$$

$$E'_f = E[Fe_{3-x}O_4] + E[Fe\ (g)] - E[Fe_3O_4] \tag{6}$$
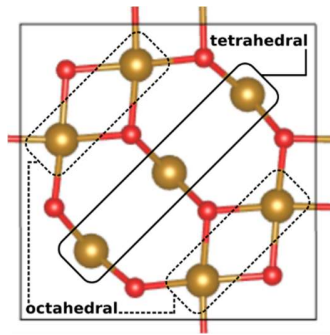
Figure S15. Top view of the first and second atomic layers of the $Fe_3O_4(001)$ unit cell. Fe atoms in octahedral and tetrahedral sites on the surface of an $Fe_3O_4(001)$ slab are marked by dashed and full lines, respectively.

Table S10. Formation energy of an iron vacancy (E_f computed with respect to solid Fe and E'_f, computed with respect to atomic Fe, in eV) and magnetic moment per unit cell (M_{total}, μ_B) on the (001) surface of Fe_3O_4.

	E_f	E'_f	M_{total}
$Fe_{3-x}O_4$ ($V_{Fe\_tetrahedral}$)	6.60	9.35	3.69
$Fe_{3-x}O_4$ ($V_{Fe\_octahedral}$)	6.64	9.39	2.08

Here, we discuss the Fe vacancy formation for the case of the most stable Pt_5/Fe_3O_4 structure (Figure 4(a)). As shown in Figure S16, there are 7 non-equivalent Fe atoms in the first and second atomic layers of the $Fe_3O_4(001)$ slab. We have considered two vacancies in tetrahedral (Fe1 and Fe2 shown in Figure S16) and two vacancies in octahedral (Fe3 and Fe4 shown in Figure S16) positions on the surface of the Pt_5/Fe_3O_4 structure. The optimized structures are shown in Figure S17.
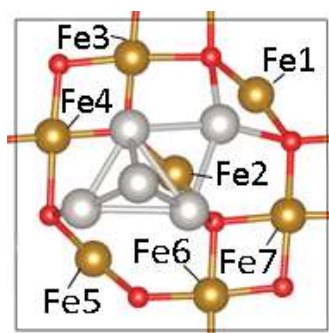
Figure S16. The non-equivalent Fe atoms in the first and second atomic layers of the Pt_5/Fe_3O_4 structure shown in Figure 4(a).
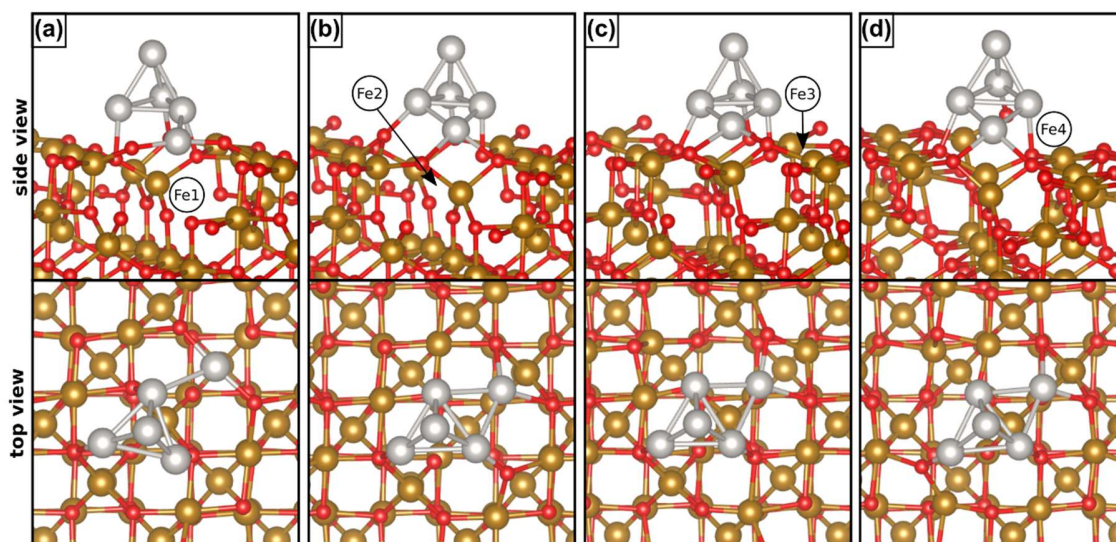
Figure S17. The optimized structures of Fe vacancies in the first layer of the Pt_5/Fe_3O_4 structure shown in Figure 4 (a).

The formation energy of the iron vacancy (E_f), given in Table S11, has been calculated according to the following equation:
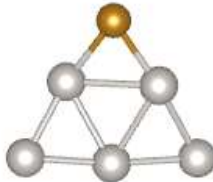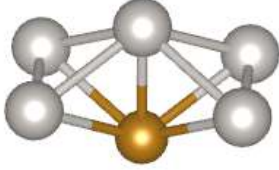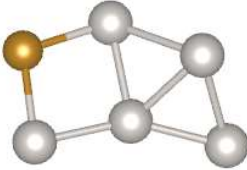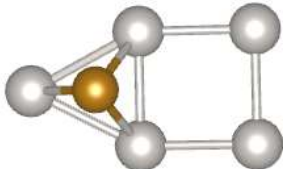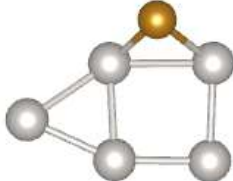
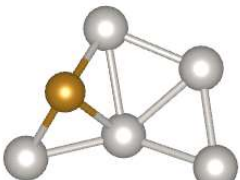$$E'_f = E[(Pt_5/Fe_{3-x}O)] + E[Fe\ (g)] - E[(Pt_5/Fe_3O_4)] \qquad (7)$$
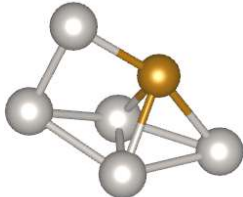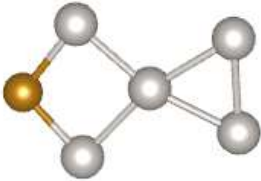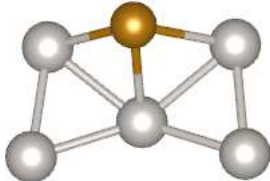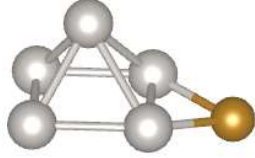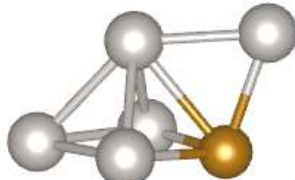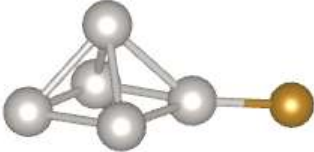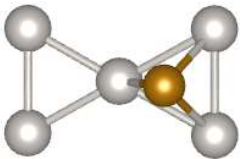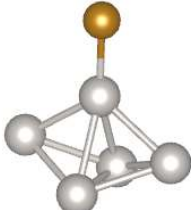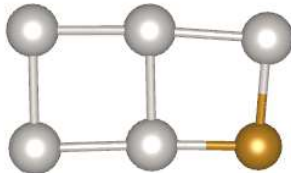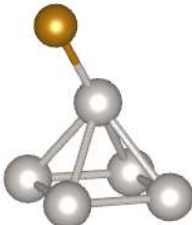
Table S11. Fe vacancy energy (E_f, eV) and total spin magnetic moment per unit cell (M, μ_B).

	Figure	E'_f	M_{total}
V_{Fe1}	S17(a)	6.70	4.84
V_{Fe2}	S17 (b)	6.90	3.64
V_{Fe3}	S17 (c)	7.69	2.52
V_{Fe4}	S17 (d)	6.37	2.87

We then consider the preferred adsorption sites for a single Fe atom on the various isomers of Pt_5 in the gas phase. Altogether, we have considered 20 possible isomers. Table S12 reports the optimized structures and their relative energy (E_R). The binding energy of Fe to Pt_5 in the most stable isomer is -0.99 eV.

Table S12. Relative energy (E_R, eV) of an adsorbed Fe atom on Pt_5 clusters.

Structure		E_R	Structure		E_R
1		0.00	11		0.82
2		0.06	12		0.95
3		0.16	13		1.04
4		0.23	14		1.10

5		0.28	15		1.49
6		0.39	16		1.76
7		0.49	17		2.39
8		0.56	18		2.71
9		0.69	19		2.74
10		0.73	20		2.76

We now consider the energetic cost of displacing the Fe1 (tetrahedral) and Fe4 (octahedral) atoms, indicated in Figure S16, from the support and adsorbing it on the Pt_5 cluster. The Fe atom has been re-adsorbed on various sites of the supported Pt_5 cluster, starting from the most stable structure (Figure 4 (a) in the main text). Figure S18 (a)-(c) and (e)-(f) shows the optimized structures. Based on our results for the Pt_5Fe gas phase isomers (Table S12), the re-adsorption of the Fe atom on the triangular facet of a supported Pt_5(i) cluster, Figure 4 (c), has also been studied. Figure S18 (d) shows the optimized structure.
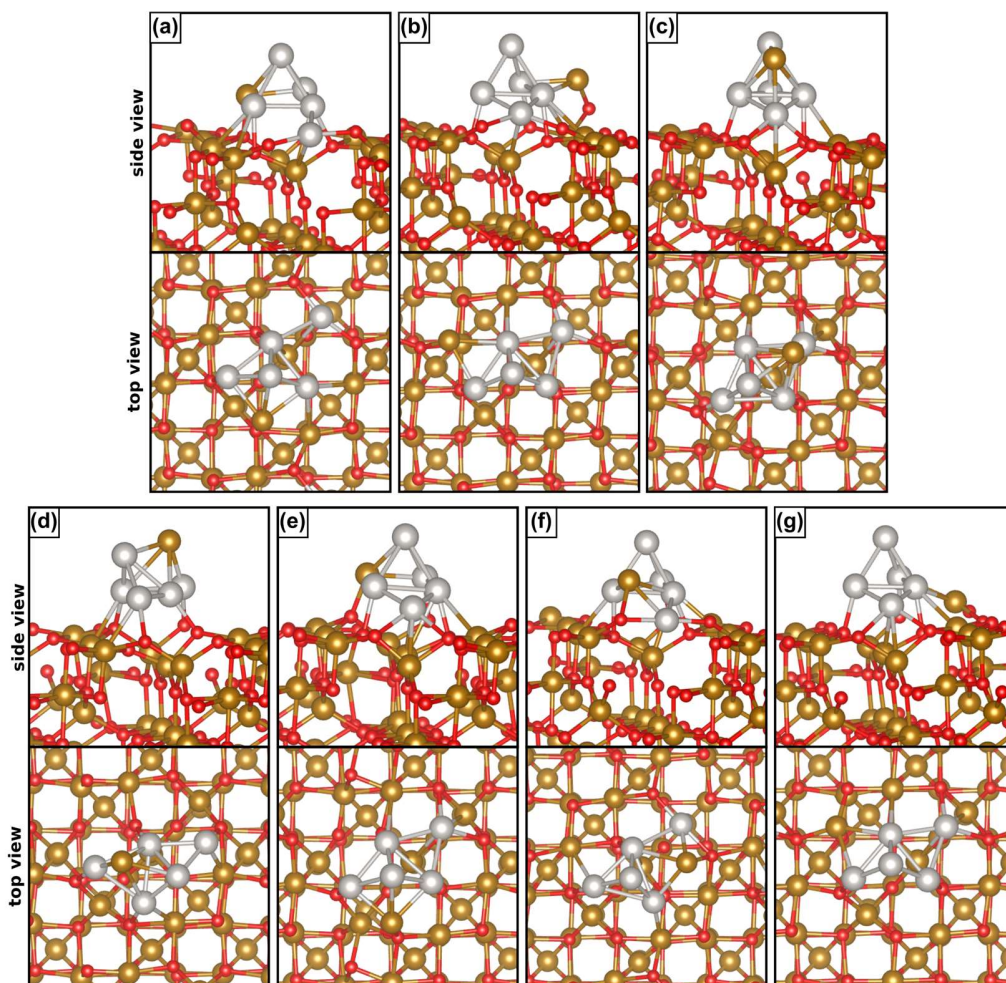

Figure S18. Various isomers of Pt_5Fe supported on Fe_3O_4.

Table S13. Fe spillover energy (E_{SO}, eV) and its site shown in Figure S16 and total spin magnetic moment per unit cell (M, μ_B).

Figure	Fe site	E_{SO}[a]	M_{total}
S18 (a)	Fe1	2.38	4.83
S18 (b)	Fe1	2.53	4.07
S18 (c)	Fe4	2.61	3.23
S18 (d)	Fe4	3.18	1.75
S18 (e)	Fe4	3.38	4.17
S18 (f)	Fe1	4.17	3.57
S18 (g) [b]	Fe4	0.14	3.24

[a] $Pt_5/Fe_3O_4 \rightarrow Fe\text{-}Pt_5/Fe_{3-x}O_4$ $\qquad \Delta E = E_{SO}$

[b] In this case, during the optimization, the Fe atom adsorbed on a triangular facet of Pt_5 moved back to the Fe_3O_4 surface.

In all cases, the Fe spillover implies a remarkable cost (between 2.38 eV and 4.17 eV, depending on the initial and final sites). Case (g) looks like an outlier displaying an almost thermoneutral formation energy, but is in fact a failed attempt, where the Fe ion spontaneously left the Pt_5 cluster and moved back to its lattice site during the relaxation.

Next, we consider the energetic cost of displacing the Fe1 (tetrahedral) or Fe4 (octahedral) atoms (see Figure S16) from the support and adsorbing them on the Pt_5O_3 cluster. The Fe atom has been re-adsorbed on the triangular facet of the supported Pt_5O_3 cluster starting from the most stable structure shown in Figure S13 (a). The results are summarized in Figure S19 and Table S14, indicating a non-favorable process.
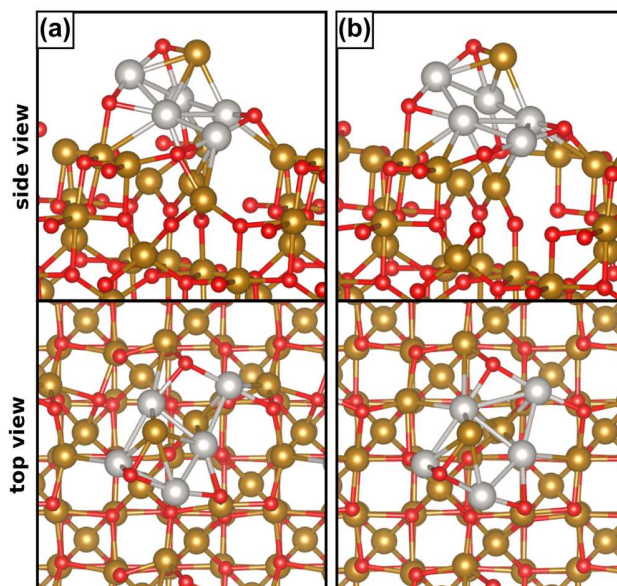
Figure S19. Various isomers of Pt_5O_3Fe supported on Fe_3O_4.

Table S14. Fe spillover energy (E_{SO}, eV) and its site shown in Figure S16 and total spin magnetic moment per unit cell (M, μ_B).

Figure	Fe site	$E_{SO}^{(a)}$	M_{total}
S19 (a)	Fe4	2.18	2.59
S19 (b)	Fe1	3.70	4.12

[a] E_{SO} refers to the process: $Pt_5/Fe_3O_4 \rightarrow Pt_5O_3Fe/Fe_{3-x}O_{4-y}$

References

(1)   Parkinson, G. S. Iron Oxide Surfaces. *Surf. Sci. Rep.* **2016**, *71* (1), 272–365.

(2)   O'Neill, H. S. C.; Dollase, W. A. Crystal Structures and Cation Distributions in Simple Spinels from Powder XRD Structural Refinements: $MgCr_2O_4$, $ZnCr_2O_4$, Fe_3O_4 and the Temperature Dependence of the Cation Distribution in ZnAl2O4. *Phys. Chem. Miner.* **1994**, *20* (8), 541–555.

(3)   Bliem, R.; McDermott, E.; Ferstl, P.; Setvin, M.; Gamba, O.; Pavelec, J.; Schneider, M. A.; Schmid, M.; Diebold, U.; Blaha, P.; Hammer, L.; Parkinson, G. S. Subsurface Cation Vacancy Stabilization of the Magnetite (001) Surface. *Science* **2014**, *346* (6214), 1215–1218.

(4)   Hulva, J.; Jakub, Z.; Novotny, Z.; Johansson, N.; Knudsen, J.; Schnadt, J.; Schmid, M.; Diebold, U.; Parkinson, G. S. Adsorption of CO on the Fe_3O_4(001) Surface. *J. Phys. Chem. B* **2018**, *122* (2), 721–729.

(5)   Zhang, K.; Shaikhutdinov, S.; Freund, H.-J. Does the Surface Structure of Oxide Affect the Strong Metal-Support Interaction with Platinum? Platinum on Fe_3O_4(001) versus Fe_3O_4(111). *ChemCatChem* **2015**, *7* (22), 3725–3730.

(6)   Kelemen, S. R.; Kaldor, A.; Dwyer, D. J. The Adsorption of CO on Clean and Potassium Promoted FeO Surfaces. *Surf. Sci.* **1982**, *121* (1), 45–60.

(7)   Sebetci, A. A Density Functional Study of Bare and Hydrogenated Platinum Clusters. *Chem. Phys.* **2006**, *331* (1), 9–18.

(8)   Xiao, L.; Wang, L. Structures of Platinum Clusters: Planar or Spherical. *J. Phys. Chem. A* **2004**, *108* (41), 8605–8614.

(9)   Yang, S. H.; Drabold, D. A.; Adams, J. B.; Ordejón, P.; Glassford, K. Density Functional Studies of Small Platinum Clusters. *J. Phys. Condens. Matter* **1997**, *9* (5), L39–L45.

(10)   Heredia, C. L.; Ferraresi-Curotto, V.; López, M. B. Characterization of Pt_N (N=2–12) Clusters through Global Reactivity Descriptors and Vibrational Spectroscopy, a Theoretical Study. *Comput. Mater. Sci.* **2012**, *53* (1), 18–24.

(11)   Bhattacharyya, K.; Majumder, C. Growth Pattern and Bonding Trends in Pt_n (n = 2-13) Clusters: Theoretical Investigation Based on First Principle Calculations. *Chem. Phys. Lett.* **2007**, *446* (4–6), 374–379.

(12)   Grönbeck, H.; Andreoni, W. Gold and Platinum Microclusters and Their Anions: Comparison of Structural and Electronic Properties. *Chem. Phys.* **2000**, *262* (1), 1–14.

(13)   Sebetci, A.; Güvenç, Z. B. Energetics and Structures of Small Clusters: Pt_N, N = 2-21. *Surf. Sci.* **2003**, *525* (1–3), 66–84.